Kinetic modelling of formation and evaporation of SOA from NO$_3$ oxidation of pure and mixed monoterpenes

Thomas Berkemeier[1,a], Masayuki Takeuchi[2], Gamze Eris[3], and Nga L. Ng[1,3]

[1]School of Chemical and Biomolecular Engineering, Georgia Institute of Technology, Atlanta, GA, USA
[2]School of Civil and Environmental Engineering, Georgia Institute of Technology, Atlanta, GA, USA
[3]School of Earth and Atmospheric Sciences, Georgia Institute of Technology, Atlanta, GA, USA
[a]now at: Multiphase Chemistry Department, Max Planck Institute for Chemistry, Mainz, Germany

Correspondence: Thomas Berkemeier (t.berkemeier@mpic.de) and Nga Lee Ng (ng@chbe.gatech.edu)

Abstract.

Organic aerosol constitutes a major fraction of the global aerosol burden and is predominantly formed as secondary organic aerosol (SOA). Environmental chambers have been used extensively to study aerosol formation and evolution under controlled conditions similar to the atmosphere, but quantitative prediction of the outcome of these experiments is generally not achieved,

5 which signifies our lack in understanding of these results and limits their portability to large scale models. In general, kinetic models employing state-of-the-art explicit chemical mechanisms fail to describe the mass concentration and composition of SOA obtained from chamber experiments. Specifically, chemical reactions involving nitrate radical (NO$_3$) oxidation of volatile organic compounds (VOCs) are a source of major uncertainty for assessing the chemical and physical properties of oxidation products. Here, we introduce a kinetic model that treats gas-phase chemistry, gas-particle partitioning, particle-phase oligomer-

10 ization, and chamber wall loss and use it to describe the oxidation of the monoterpenes α-pinene and limonene with NO$_3$. The model can reproduce aerosol mass and nitration degrees in experiments using either pure precursors or their mixtures and infers volatility distributions of products, branching ratios of reactive intermediates as well as particle-phase reaction rates. The gas-phase chemistry in the model is based on the Master Chemical Mechanism (MCM), but trades speciation of single compounds for the overall ability of quantitatively describing SOA formation by using a lumped chemical mechanism. The

15 complex branching into a multitude of individual products in MCM is replaced in this model with product volatility distributions, detailed peroxy (RO$_2$) and alkoxy (RO) radical chemistry and amended by a particle-phase oligomerization scheme. The kinetic parameters obtained in this study are constrained by a set of SOA formation and evaporation experiments conducted in the Georgia Tech Environmental Chamber (GTEC) facility. For both precursors, we present volatility distributions of nitrated and non-nitrated reaction products that are obtained by fitting the kinetic model systematically to the experimental data using

20 a global optimization method, the Monte Carlo Genetic Algorithm (MCGA). The results presented here provide new mechanistic insight into the processes leading to formation and evaporation of SOA. Most notably, much of the non-linear behavior of precursor mixtures can be understood by RO$_2$ fate and reversible oligomerization reactions in the particle phase, but some effects could be accredited to kinetic limitations of mass transport in the particle phase. The methodologies described in this work provide a basis for quantitative analysis of multi-source data from environmental chamber experiments with manageable

25 computational effort.

1 Introduction

Atmospheric aerosol particles play an important role in the Earth system by influencing weather and climate, enabling long-range transport of chemical compounds, and negatively affecting public health (Pöschl, 2005; Fuzzi et al., 2006). A major contributor to the global aerosol burden is the oxidation of volatile organic compounds (VOCs) to condensable organic species,

30 which leads to formation of secondary organic aerosol (SOA; Kanakidou et al., 2005). Important classes of SOA precursors include alkanes and aromatic compounds, which are often emitted from anthropogenic sources, as well as alkenes such as isoprene, monoterpenes, and sesquiterpenes, which are predominantly emitted by trees (Hallquist et al., 2009). The monoterpenes α-pinene and limonene are among the most abundant and well-studied SOA precursors (Seinfeld and Pandis, 2016). Atmospheric oxidation of alkenes occurs mainly through three oxidants: the hydroxyl radical (OH), which is produced in daylight

35 and is short-lived; the abundant, but comparatively slow reacting ozone (O_3); and the nitrate radical (NO_3), which is the major source of SOA at nighttime, but also contributes to SOA formation during daytime, despite its quick photolysis (Liebmann et al., 2019). The oxidation of VOCs by NO_3 results in the formation of high yields of nitrated organic compounds, alkyl nitrates and peroxy acyl nitrates, which are produced in lower quantities through other atmospheric oxidation channels such as reaction of organic peroxy radicals (RO_2) with nitric oxide (NO) (Perring et al., 2013; Ng et al., 2017). These organic nitrates

40 (ON) play an important role in the atmospheric nitrogen budget by serving as temporary or permanent sink for highly reactive nitrogen oxides (NO, $NO_2 = NO_x$). Reactive nitrogen oxides constitute an integral part of oxidation cycles in the atmosphere and are made significantly less reactive through reaction to ON.

Due to their sufficiently low volatility, ON can be taken up into atmospheric aerosol particles, where they are shielded from gas-phase chemical decomposition, causing NO_x to be temporarily removed from atmospheric oxidation cycling. While

45 NO_x can be recycled back into the atmosphere via photolysis (Müller et al., 2014), photooxidation (Nah et al., 2016), and thermal decomposition of ON, permanent removal can occur through ON hydrolysis (Takeuchi and Ng, 2019) and deposition processes (Nguyen et al., 2015).

Furthermore, the presence of ON affects the formation and persistence of organic aerosol (OA) (Ng et al., 2017). The contribution of particulate ON mass (pON) to total organic aerosol has been investigated previously in laboratory studies by

50 mass-spectrometric methods (Fry et al., 2009, 2011, 2014; Boyd et al., 2015; Nah et al., 2016; Boyd et al., 2017; Faxon et al., 2018; Takeuchi and Ng, 2019) and a radioactive tracer method (Berkemeier et al., 2016), revealing that organic nitrate mass fractions can reach up to 0.8 in the particle phase under certain conditions. Although ambient measurements varied strongly temporally and regionally, the ratio of ON mass to the total organic mass has been shown to reach up to 0.77 (Ng et al., 2017, and references therein).

55 Despite the importance of ON to the dynamics of SOA formation, the chemical mechanism for their formation in the gas and particle phases is still under discussion (Kurtén et al., 2017; Claflin and Ziemann, 2018; Draper et al., 2019). The Master Chemical Mechanism (MCM) provides a resource of the gas phase degradation chemistry of typical SOA precursors with atmospheric oxidants (Saunders et al., 2003; Jenkin et al., 2003). However, application of MCM to the oxidation of

monoterpenes with NO_3 leads to a significant underestimation of particle mass and pON/OA (Boyd et al., 2017; Faxon et al.,

60   2018).

It has been hypothesized and shown recently that a majority of SOA might exist in oligomerized form (Kalberer et al., 2004; Gao et al., 2010), which might alter their evaporation behavior (Baltensperger et al., 2005; D'Ambro et al., 2018). In that case, the evaporation time scale is determined by chemical decomposition instead of equilibrium partitioning due to volatility (Pankow, 1994). Additionally, organic aerosol particles can exhibit a highly viscous phase state (Virtanen et al.,

65   2010; Koop et al., 2011; Reid et al., 2018), which leads to kinetic limitations in evaporation (Vaden et al., 2011), reduced particle-phase chemistry (Gatzsche et al., 2017), and non-equilibrium partitioning (Cappa and Wilson, 2011).

To describe kinetic limitations in mass transport, a number of kinetic multi-layer models have been developed recently to describe aerosol particles and cloud droplets, including KM-SUB (Shiraiwa et al., 2010), KM-GAP (Shiraiwa et al., 2012), ADCHAM (Roldin et al., 2014), and MOSAIC (Zaveri et al., 2008, 2014). These models are capable of explicitly resolving

70   mass transport and chemical reactions within aerosol particles. Using these models, Shiraiwa et al. (2013) and Zaveri et al. (2018) were able to find evidence for diffusion limitation affecting SOA formation dynamics by inspection of the evolution of particle size distributions. Yli-Juuti et al. (2017) and Tikkanen et al. (2019) used an evaporation model based on KM-GAP to describe the interaction of volatility and viscosity during isothermal dilution as a function of different environmental conditions. However, to our best knowledge, no model has been presented that describes all aspects of gas-phase chemistry, particle-phase

75   chemistry, gas-particle partitioning and bulk diffusion of SOA.

A model capable of describing all these aspects of SOA formation must rely on a large set of kinetic parameters, which are often not readily accessible. However, model parameters can be systematically altered so the model matches experimental data, an approach often referred to as inverse modelling. Simultaneously optimizing multiple model parameters can often be unfeasible via manual optimization and prompts the use of global optimization methods (Berkemeier et al., 2013, 2017). As

80   opposed to local optimization methods, global optimization algorithms are not as easily stuck in local minima and are able to reliably find solutions of difficult optimization problems. In conjunction with a kinetic model, global optimization algorithms represent a powerful tool that allows to infer molecular level information from macroscopic data. Thus, global optimization algorithms based on differential evolution, such as the Monte Carlo Genetic Algorithm (MCGA), have become increasingly popular in the modelling of complex multiphase chemical systems (Berkemeier et al., 2017; Marshall et al., 2018; Tikkanen

85   et al., 2019).

In a previous study, Boyd et al. (2017) showed that the retained aerosol mass from oxidation of limonene with NO_3 after heating from 25 °C to 40 °C is significantly different than the mass obtained from oxidizing limonene at 40 °C. They further showed that the evaporation behavior of mixtures of limonene SOA and β-pinene SOA crucially depends on the order in which oxidation occurred. Limonene SOA evaporated less in the experiment where oxidation of limonene was followed by

90   oxidation of β-pinene, compared to the experiment where both precursors were oxidized simultaneously. At the time, it was only postulated that diffusion limitations and/or oligomerization reactions could have led to these observations. In this work, we conduct new environmental chamber experiments and apply a novel kinetic modelling framework to investigate whether gas-phase chemistry, equilibrium partitioning, and particle-phase chemistry can describe the formation and evaporation of

monoterpene SOA from oxidation of α-pinene, limonene, and mixtures of both precursors with NO_3. α-pinene is chosen
over β-pinene since it shows a more distinct evaporation behavior to limonene SOA and is the overall better-understood SOA
precursor. We perform experiments at a lower initial temperature compared to Boyd et al. (2017) to include a second heating
stage in the experiments. We focus the modelling efforts on the experimental observables aerosol mass and organic nitrogen
content (contribution of particulate ON mass to total organic aerosol, pON/OA) as a function of time in the reaction chamber.
We apply a kinetic model that uses a simplified, lumped kinetic mechanism based on MCM (Berkemeier et al., 2016), but
modifies some of the branching ratios in RO_2 chemistry and adds chemical reactivity in the particle phase. Building on the
observations of Boyd et al. (2017) in their mixed precursor experiments, we investigate the linearity of these two observables
by quantitative comparison of formation and evaporation of SOA from pure and mixed monoterpene precursors. Lastly, we
use the kinetic model to perform a sensitivity analysis on the potential effect of retarded bulk diffusion due to a viscous phase
state. The kinetic modelling framework consisting of a kinetic multi-layer model based on KM-GAP and the MCGA algorithm
is used as analysis tool to unravel the mechanistic interactions between reactive intermediates and oxidation products that can
lead to non-additivity of the investigated reaction systems.

2   Experimental and theoretical methods

2.1   Georgia Tech Environmental Chamber (GTEC)

The aerosol formation and evaporation experiments are performed as batch reactions in the GTEC facility, which consists of
two separate 12 m^3 Teflon chambers in a temperature- and humidity-controlled enclosure (Boyd et al., 2015). A consistent
experimental routine is maintained for all experiments presented in this study and resembles the method used by Boyd et al.
(2017) with small updates. Concentrations of O_3 and NO_x are determined with a UV absorption O_3 analyzer (Teledyne T400)
and a chemiluminescence NO_x monitor (Teledyne 200 EU), respectively. Aerosol particle number and volume concentrations
are measured using a scanning mobility particle sizer (SMPS, TSI), which consists of a differential mobility analyzer (DMA,
TSI 3040) and a condensation particle counter (CPC, TSI 3775). Bulk aerosol composition is measured using a High Resolution
Time-of-Flight Aerosol Mass Spectrometer (HR-ToF-AMS, DeCarlo et al., 2006).

The Teflon chamber is flushed with zero air for at least 24 h and the chamber enclosure is cooled to 5 °C several hours prior
to each experiment, to ensure full equilibration with regard to temperature, pressure, and humidity. Monoterpene oxidation is
initiated at 5 °C and under dry conditions (RH < 5 %). All experiments are conducted using ammonium sulfate seed parti-
cles. Seed particles are generated by atomizing a 15 mM ammonium sulfate solution into the chamber for 20 minutes, which
typically results in particle number concentrations around 20 000 cm^{-3} and mass concentrations of 28 – 41 μg/m^3. Simul-
taneously, monoterpene precursors are injected into the chamber. Injection volumes of the precursors are chosen to achieve
consistent total aerosol mass concentrations around 100 μg/m^3 in all experiments, based on knowledge about aerosol yields in
trial experiments for this study. For α-pinene, we use a micro syringe to inject a known volume of liquid into a mildly heated
glass bulb from which a 5 L/min zero air flow carries the evaporating fumes into the chamber. For limonene, the required
liquid volume is so low that the use of micro syringes is a source of non-negligible uncertainty and hence a gas cylinder filled

with 0.85 ppm limonene, calibrated and confirmed using gas chromatography with flame ionization detection (GC-FID), is used to inject a known volume of gas into the chamber over the course of several minutes. NO_3 is produced by oxidation of NO_2 with O_3 (generated by passing zero air through a photochemical ozone generator) in a 1.5 L flow tube (0.9 L/min flow,

130   100 s residence time). The reaction mixture is optimized so NO_3 and N_2O_5 are produced in high yields, with no significant amount of O_3 entering the chamber. This is achieved by using a 2:1 ratio of NO_2 and O_3. N_2O_5 decomposes in the chamber to release NO_3 over time. Injection of NO_3/N_2O_5 marks the beginning of the reaction.

When peak SOA growth is reached, which is typically achieved in under 4 hours of the experiment, the chamber enclosure temperature is raised to 25 °C and, after another waiting period, to 42 °C. The temperature changes take approximately 90

135   minutes in both cases. Temperature profiles are reported alongside the experimental results in Fig. 2.

In total, four experiments are conducted, either with a single monoterpene precursor, pure α-pinene (APN) and pure limonene (LIM), or with a mixture of both precursors. In the case where both precursors are used, the oxidation occurred in one of two variants: simultaneous (MIX) or sequential oxidation (SEQ). In case of the MIX experiment, both precursors are injected simultaneously into the chamber prior to NO_3/N_2O_5 injection. In case of the SEQ experiment, peak growth of the first precursor

140   oxidation is first awaited. The first oxidation is followed by a second NO_3/N_2O_5 injection and injection of the second VOC precursor shortly thereafter. An 8-fold excess of N_2O_5 is used for pure limonene experiments, and a 4-fold excess used for pure α-pinene experiments. In the mixed precursor experiments, the amount of injected NO_3/N_2O_5 is determined using the same ratios proportionately. A summary of all experimental conditions, including injected precursor amounts, aerosol mass, organic aerosol mass excluding seed, and SOA yields can be found in Table 1. It is noted that we refer to the total aerosol

145   mass concentration (sum of inorganic seed mass concentration and organic aerosol mass concentration) in the chamber simply as "aerosol mass" in our discussions. "SOA yield" refers to the ratio of produced organic aerosol mass to the reacted VOC mass (Odum et al., 1996).

2.2   Kinetic model

The kinetic model calculations in this study are performed with a multi-compartmental model akin to the KM-SUB/KM-

150   GAP model family (Shiraiwa et al., 2010, 2012). The model code is set up as a generator script that uses an input chemical mechanism to generate a system of differential equations that is able to describe the key physical and chemical processes in the GTEC chamber. The model compartments include the chamber wall, the chamber gas phase, the particle near-surface gas phase, the particle surface and the particle bulk. The processes explicitly described in the model include injection of chemical compounds, wall loss of gas phase species, temperature change, gas diffusion to particles, condensation and evaporation at the

155   particle surface, as well as chemical reaction in the gas and particle phases. Wall loss of particles is implicitly accounted for in this study by using wall loss-corrected SMPS data (Keywood et al., 2004; Nah et al., 2017).

All product molecules with volatility lower than 10^{-5} Pa are allowed to partition into the topmost layer of the particles. Gas-particle partitioning is explicitly treated in the model and equilibration between the particle near-surface gas phase and the particle surface is achieved by balancing surface adsorption and desorption rates. This way, evaporation and condensation

160   kinetics are treated more realistically than in a model assuming instantaneous equilibrium partitioning. The adsorption flux

$J_{\mathrm{ads},X}$ of a molecule X is calculated from the collision flux from the particle near-surface gas phase to the particle surface, which in turn is calculated from the mean thermal velocity ω_X and the accommodation coefficient $\alpha_{\mathrm{s},X}$. $\alpha_{\mathrm{s},X}$ is assumed to be 0.1 for all organic species in this study, in line with previous investigations (Julin et al., 2013).

$$J_{\mathrm{ads},X} = \alpha_{\mathrm{s},X} \cdot \frac{\omega_X}{4} \cdot [X]_{\mathrm{gs}} \tag{1}$$

165 The desorption flux from the particle surface to the gas phase $J_{\mathrm{des},X}$ is dependent on the vapor pressure $p_{\mathrm{vap},X}$ and the ratio of the concentration of X in the particle near-surface bulk layer $[X]_{\mathrm{b1}}$, and the sum of all other species Y_{j} in that layer.

$$J_{\mathrm{des},X} = \frac{\alpha_{\mathrm{s},X} \cdot \omega_X \cdot p_{\mathrm{vap},X} \cdot N_{\mathrm{A}} \cdot [X]_{\mathrm{b1}}}{4 \cdot R \cdot T \cdot \sum [Y_j]_{\mathrm{b1}}} \tag{2}$$

Here, R is the universal gas constant, T the temperature in K, and N_{A} is Avogadro's number. The vapor pressure of product compounds is assumed to be temperature dependent with a precursor-dependent effective enthalpy of volatilization, $\Delta H_{\mathrm{vap},Z}$

170 in $\mathrm{kJ/mol}$, where Z is the precursor of X. We assume this single effective enthalpy to be temperature independent and representative for the entire product spectrum.

$$p_{\mathrm{vap},X}(T) = p_{\mathrm{vap},X}(298\ \mathrm{K}) \cdot \exp \frac{-\Delta H_{\mathrm{vap},Z}}{R \cdot (T - 298)} \tag{3}$$

Note that in this study only a single well-mixed layer is used to describe the aerosol phase. New particle formation from low-volatility vapors is not treated in this model, so seed particles have to be pre-defined. Seed particles are initialized as covered

175 with a very small amount of non-volatile organics (5×10^{-3} ppb gas-phase mixing ratio) to aid in computation of gas-particle partitioning. The model can be run in two modes: lumped mode, in which only vapor pressure bins are defined, and explicit mode, in which vapor pressures must be pre-supplied for all participating species. In the following, we will describe the specific lumped mode used in this study.

2.3 Lumped chemical mechanism

180 The gas-phase chemical mechanism, summarized in Fig. 1a, is modeled after the initial reaction steps in the MCM, but does not assume specific sum or structural formulas of product molecules. The validity of this approach has been shown in previous work (Berkemeier et al., 2016). For limonene SOA, we apply the same general chemistry, but consider the oxidation of both double bonds individually, which leads to the more complex reaction scheme shown in Fig. S1. Note that oxidation of the second double bond of limonene with NO_3 is not considered in MCM, which makes the reaction mechanism distinctly different

185 to the MCM template. However, we have shown previously that including oxidation of the second double bond leads to a significantly improved correlation between a kinetic model and chamber experiments (Boyd et al., 2017).

To account for chemical identity, the major product classes, nitrated and non-nitrated organic molecules, are subdivided into volatility bins (Fig. 1b) following the concept of a volatility basis set (VBS; Donahue et al., 2011). The six volatility bins employed in this study are chosen to have increased resolution and hence achieve maximum sensitivity around the ex-

190 perimental range of $10 - 100\ \mathrm{\mu g/m^3}$, but still cover a wider range of volatilities: (1) 1.32×10^{-12} Pa ($C^* = 0.01\ \mathrm{\mu g/m^3}$), (2) 1.32×10^{-10} Pa ($C^* = 1\ \mathrm{\mu g/m^3}$), (3) 1.32×10^{-9} Pa ($C^* = 10\ \mathrm{\mu g/m^3}$), (4) 1.32×10^{-8} Pa ($C^* = 100\ \mathrm{\mu g/m^3}$), (5)
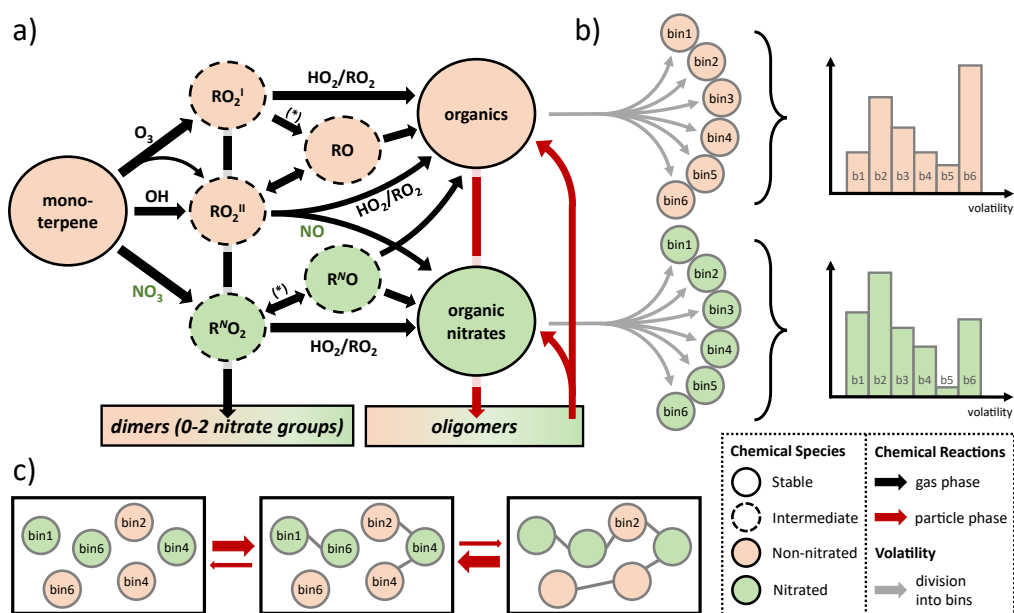
Figure 1. (a) Schematic representation of the lumped chemical mechanism for oxidation of monoterpenes with one double bond (e.g., α-pinene). The asterisk stands for chemical reaction with NO, NO_3, and RO_2. (b) The stable products are divided into 6 product bins each with a different volatility (grey arrows; bin1-bin6), according to a probability distribution (exemplary graphs on the right). (c) Oligomerization occurs in equilibrium reactions in the particle phase under conservation of precursor origin and volatility bin.

1.32×10^{-7} Pa ($C^* = 1000$ µg/m^3) and (6) 1.32×10^{-5} Pa ($C^* = 100\,000$ µg/m^3) at 298 K. C^* is the saturation mass concentration, which indicates the organic aerosol mass at which a semi-volatile organic substance would be in the gas and particle phase in equal parts. Note that while C^* is temperature dependent, we refer to the moving volatility bins in this
195 manuscript by their C^* at 298 K.

Oligomeric species are chosen to be fully non-volatile and hence technically form a seventh volatility bin. The average molar mass of molecules in the organic aerosol phase is assumed to be 250 g/mol, which is similar to assumptions in previous publications(Berkemeier et al., 2016) and consistent with our measurements using chemical ionization high-resolution time-of-flight mass spectrometry with a special filter inlet that samples both the aerosol and gas phase (FIGAERO-HRToF-CIMS
200 Lopez-Hilfiker et al., 2014) that were conducted alongside this study (Takeuchi and Ng, 2019).

A specific aim of this study is the mechanistic analysis of ON formation. Therefore, the gas-phase formation of ON is treated in detail and has been expanded from the MCM template, which is detailed in Fig. S2. We assume that chemical reaction of NO_3 with the terpenic precursor yields a nitrated peroxy radical ($R^N O_2$). The fate of the nitrate group (-ONO_2) in this radical is dependent on its radical branching ratios. Following MCM, we assume that the reaction of $R^N O_2$ with HO_2 yields a stable
205 organic nitrate product, whereas reaction with NO, NO_3, RO_2, or unimolecular decay leads to formation of a nitrated alkoxy radical ($R^N O$), which can further stabilize under elimination of the nitrate group. Reaction of two RO_2 may also yield dimers.

Another channel of ON formation is the reaction of a non-nitrated peroxy radical (RO_2^{II}) with NO. Following MCM, we assume that only RO_2^{II}, which is the main intermediate in monoterpene OH oxidation and a secondary intermediate of monoterpene ozonolysis, can undergo this reaction. It is hence distinct from RO_2^{I}, which is the main intermediate in monoterpene ozonolysis.

210 However, this RO_2^{II} + NO reaction channel has only minor implications in this study due to the low prevalence of NO under the employed reaction conditions, i.e., injection of NO_3/N_2O_5 as well as no irradiance with UV lights.

Particle-phase chemistry is included as formation and decomposition of oligomers from monoterpene oxidation products. Possible reaction pathways for oligomerization include the formation of esters, aldols, hemiacetals, acetals, peroxyhemiacetals, and peroxyacetals from alcohol, aldehyde, hydroperoxide, and carboxylic acid moieties in the monoterpene oxidation

215 products (Ziemann and Atkinson, 2012), but are lumped into a single reaction for simplicity. These oligomers are assumed to be non-volatile, but can re-partition back to the gas phase after decomposition into the monomeric building blocks. Oligomer decomposition is treated as temperature dependent with a precursor-specific activation energy $E_{A,decom,Z}$ to be used in an Arrhenius equation. The information about volatility and nitration degree of monomers is retained during oligomerization and reinstated after their decomposition. This process is outlined in Fig. 1c. A detailed discussion of the oligomerization scheme

220 is provided in the Supplement, Sect. S1 and Fig. S3. An overview of all reactions of the lumped model in the gas and particle phases is given in Table S1.

2.4 Global optimization

The Monte Carlo Genetic Algorithm (MCGA; Berkemeier et al., 2017) is applied for inverse fitting of the kinetic model to the experimental data and determining the non-prescribed kinetic parameters listed in Table 1. The MCGA method consists of

225 two steps: a Monte Carlo step and a genetic algorithm step. During the Monte Carlo step, kinetic parameter sets are randomly sampled from a defined parameter range and the residue between the model result and the experimental data is determined for each parameter set through evaluation of the kinetic model. During the genetic algorithm step, the parameter sets are optimized mimicking processes known from natural evolution: a survival mechanism retains best-fitting parameter sets, the recombination mechanic generates new parameter sets by combing parameters of high scoring sets, and the mutation step

230 prevents early homogenization of the sample of parameter sets. To determine the model-experiment correlation, we use a weighted mean squared error (wMSE) approach that minimizes the sum of the squares of the residuals, Eq. 4. The estimator is normalized to the magnitude of the largest data point in a given sample, $\max(Y_{,i})$, and the number of data points n_i of data set i. Additionally, optional weighting factors w_i can be used to guide the optimization process.

$$\text{wMSE}_i = w_i \sqrt{\frac{1}{n_i} \sum \left(\frac{Y_{\text{model}} - Y_{\text{data},i}}{\max(Y_{\text{data},i})} \right)} \tag{4}$$

235 After an optimization result is returned, a 1-dimensional golden-section search (Press et al., 2007, Sect. 10.2) is used to ensure conversion into a minimum of the optimization hypersurface. The simplex method (Press et al., 2007, Sect. 10.5) is used to find other combinations of parameters that lead to equivalent model results (test of uniqueness). Weighting factors w_i can be used to assign a lower importance to data sets that e.g., exhibit large scatter due to experimental noise, represent experimental artifacts or are deemed only supplementary for the purpose of the optimization.

Table 1. Fit parameters of the kinetic model. Error estimates for the volatility distribution (parameters f_{apin} and f_{lim}) can be found in Fig. S5 in the supplement, error estimates for all other parameters are ranges in which a parameter can be varied until the model-experiment correlation decreases by 10 %. For a full list of kinetic parameters, see Table S1.

Parameter	Value of best fit	Description
$f_{apin,org,b1} - f_{apin,org,b6}$	see Fig. S5	Volatility distribution of non-nitrated α-pinene oxidation products
$f_{apin,nitr,b1} - f_{apin,nitr,b6}$	see Fig. S5	Volatility distribution of nitrated α-pinene oxidation products
$f_{lim,org,b1} - f_{lim,org,b6}$	see Fig. S5	Volatility distribution of non-nitrated limonene oxidation products
$f_{lim,nitr,b1} - f_{lim,nitr,b6}$	see Fig. S5	Volatility distribution of nitrated limonene oxidation products
gpwl	$2.80\ (2.31 - 3.34)\ \times 10^{-7}$	Gas-phase wall loss rate
$\Delta H_{vap,apin}$	76.7 (62.9 – 88.5)	Effective enthalpy of vaporization of α-pinene SOA products (kJ/mol)
$\Delta H_{vap,lim}$	69.2 (66.0 – 72.2)	Effective enthalpy of vaporization of limonene SOA products (kJ/mol)
$p_{vap,IM1}$	$2.06\ (1.38 - 4.70)\ \times 10^{-7}$	Vapor pressure, non-nitrated limonene SOA intermediate (Pa)
$p_{vap,IM2}$	$3.86\ (3.16 - 4.48)\ \times 10^{-8}$	Vapor pressure, nitrated limonene SOA intermediate (Pa)
c_1	$1.39\ (1.06 - 1.68)\ \times 10^{-2}$	Branching ratio, gas-phase dimer yield from $RO_2 + RO_2$
c_2	0.141 (0.102 - 0.171)	Branching ratio, RO yield from $RO_2 + RO_2$
$c_{3,apin}$	$6.91\ (6.30 - 7.46)\ \times 10^{-2}$	Branching ratio, product yield from RO, α-pinene
$c_{3,lim}$	0.774 (0.578 – 0.972)	Branching ratio, product yield from RO, limonene
$c_{4,apin}$	$0\ (0 - 9.65)\ \times 10^{-2}$	Product ratio of non-nitrated to nitrate ratio species from RO, α-pinene
$c_{4,lim}$	0.230 (0.190 – 0.272)	Product ratio of non-nitrated to nitrate ratio species from RO, limonene
$k_{form,apin}$	17.4 (9.5 – 27.0)	Oligomerization rate coefficient, α-pinene (h^{-1})
$k_{form,lim}$	1.11 (1.01 – 1.22)	Oligomerization rate coefficient, limonene (h^{-1})
$k_{decom,apin}$	3.28 (2.13 – 6.04)	Oligomer decomposition rate coefficient, α-pinene (h^{-1})
$k_{decom,lim}$	$3.92\ (3.56 - 4.28)\ \times 10^{-2}$	Oligomer decomposition rate coefficient, limonene (h^{-1})
$E_{A,decom,apin}$	620 (492 – 801)	Activation energy of oligomer decomposition, α-pinene (kJ/mol)
$E_{A,decom,lim}$	244 (214 – 269)	Activation energy of oligomer decomposition, limonene (kJ/mol)

240   Note that for the experiments discussed in this manuscript, multiple model solutions can be obtained, dependent not only on the choice of data sets that is optimized to, but also on the choice of weighting factors. In the following sections, only one fit of the model to experimental data will be discussed as de-facto fit as it scored best in our choice of the model-experiment correlation estimator. The fit is obtained by fitting to total aerosol mass and aerosol organic nitrate fraction (pON/OA) data of three experimental data sets (LIM, APN, and SEQ). The fourth experiment (MIX) is intentionally left out from the fitting

245   process for cross-validation. We will discuss the dependence of the best fit on weighting factors and the uniqueness of the obtained model solution in a separate section, Sects. 3.4 and 4.

Table 2. Experimental conditions for environmental chamber experiments presented in this study alongside aerosol masses and SOA yields during peak growth at 5 °C.

Exp	VOC 1 (ppb)	VOC 2 (ppb)	Experiment variant	Seed mass† ($\mu g/m^3$)	Peak aerosol mass† ($\mu g/m^3$)	Peak OA mass† ($\mu g/m^3$)	SOA yield (%)
LIM	limonene (10.5 ± 1.1)		pure limonene	28.8 ± 1.4	110.1 ± 5.5	81.3 ± 5.7	129.6 ± 15.8
APN	α-pinene (47.5 ± 4.8)		pure α-pinene	37.3 ± 1.9	108.7 ± 5.4	71.4 ± 5.7	25.2 ± 3.2
SEQ	α-pinene (24 ± 2.4)	limonene (5 ± 0.5)	sequential	33.4 ± 1.7	100.1 ± 5.0	66.7 ± 5.3	38.5 ± 4.9
MIX	α-pinene (22.5 ± 2.3)	limonene (5 ± 0.5)	simultaneous	40.9 ± 2.0	93.8 ± 4.7	52.9 ± 5.1	32.2 ± 4.5

$\dagger$: Aerosol masses are calculated from aerosol volume concentrations using a density of the organic phase of 1.64 g/cm^3 for limonene SOA (Boyd et al., 2017), 1.46 g/cm^3 for α-pinene SOA (Nah et al., 2016), and 1.55 g/cm^3 for the mixtures. All reported masses are particle wall-loss corrected.

3 Results and discussion

3.1 Pure limonene oxidation (LIM)

3.1.1 Experimental observations (LIM)

250 Fig. 2a shows the total aerosol mass concentration (denoted as "aerosol mass") during an experiment of limonene oxidation with NO$_3$ in the presence of ammonium sulfate seed particles, and subsequent evaporation in the GTEC chamber, here referred to as "LIM" experiment. Oxidation at 5 °C initially causes a fast increase in aerosol mass (black open markers, left axis) from 29 $\mu g/m^3$ of seed mass to about 70 $\mu g/m^3$ of aerosol mass within the first 20 minutes of the experiment. Afterwards, aerosol growth slows down considerably, so that the peak aerosol mass of 110 $\mu g/m^3$ is reached only after 5 hours. The slow increase
255 in aerosol mass in the beginning of the experiment is likely an important feature of the experimental data for determination of mass transfer and chemical reaction rates.

The produced aerosol mass corresponds to a SOA yield of 130 % (Table 2) and is observed to be constant in the chamber for several hours at 5 °C. Note that this observation is different from previous experiments conducted at 25 °C and 40 °C (Boyd et al., 2017), where peak aerosol mass was achieved swiftly and SOA yields at aerosol mass loading similar to this study were
260 determined to be 174 % (yield constant with mass loading) and 124 %, respectively. While the lower SOA yield at 40 °C compared to 25 °C can be explained with equilibrium partitioning theory, the lower mass yield observed at 5 °C in this study cannot.

After 7 hours of total experiment time, the temperature set point of the chamber enclosure is increased to 25 °C. The new temperature plateau is reached inside the Teflon chamber 90 minutes later (grey dashed line, right axis). The temperature
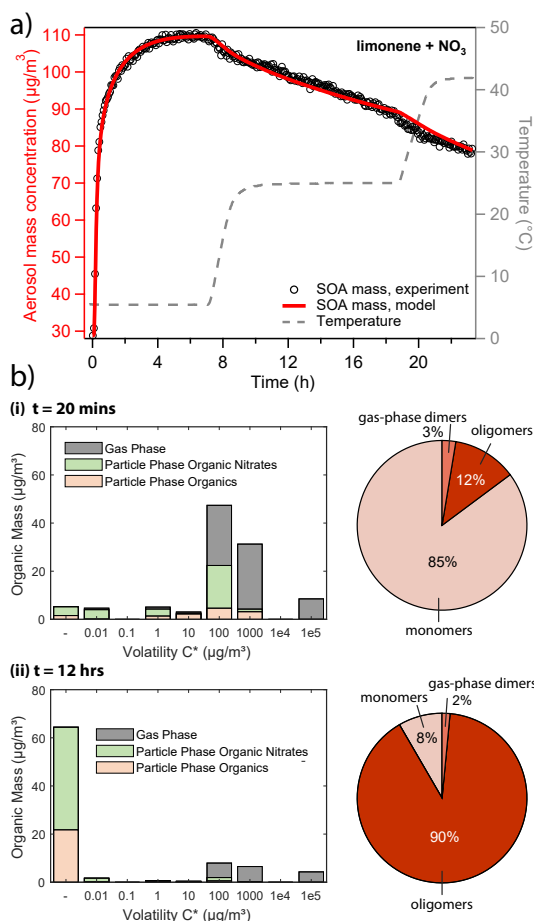
Figure 2. (a) Comparison of experimental and modelling results for oxidation of limonene with NO_3. Open black markers are experimental aerosol mass obtained using an SMPS. The red solid line represents the model result and the grey dashed line corresponds to the experimental temperature profile. (b) Analysis of the occupation of volatility bins of all products (bar plot) and oligomerization state of particle-phase products (pie chart) in the model (i) 20 minutes and (ii) 12 hours after the beginning of the experiment. Shadings in the bar plot denote where molecules of a certain volatility bin reside: gas phase (grey) or particle phase (colored). Products in the particle phase are further distinguished as ON (green) and non-nitrated organics (orange).

265 change causes a slight reduction in aerosol mass from 110 to about 104 $\mu g/m^3$. At the new temperature set point, aerosol mass is not constant, but rather decays at a constant rate. After about 19 hours, the temperature set point is increased to 42 °C, which again causes an immediate slight reduction in aerosol mass from 90 to about 83 $\mu g/m^3$. At the new temperature plateau of 42 °C, aerosol mass once again decays at a constant rate that is comparable to the one previously observed.

3.1.2 Kinetic modelling results (LIM)

270 In the following, kinetic modelling results are discussed in terms of a best fit that is obtained using the Monte Carlo Genetic

Algorithm (MCGA). The uniqueness of this fit and potential pitfalls of the optimization process are discussed in Sects. 3.4

and 4. The kinetic model (red solid line in Fig. 2a) is able to reproduce the observed aerosol formation and evaporation

behavior. In the model run at hand, the initial quick increase in aerosol mass is due to condensation of dimers formed in the gas

phase through the $RO_2 + RO_2$ channel (from now on referred to as "gas-phase dimers"), making up about 50 % of condensing

275 material in the initial seconds and minutes. Subsequent growth is due to condensation of monomeric oxidation products (from

now on referred to as "monomers") of sufficiently low volatility. After 20 minutes, half of the aerosol mass at peak growth is

reached and the particle phase is mostly comprised of monomers, cf. Fig. 2b, panel (i), about one third of which still contain

an C-C double bond (Fig. S4). These mono-unsaturated oxidation products either partition back into the gas phase where they

can be oxidized further, or co-oligomerize in the particle phase with other products. The vapor pressure of the non-nitrated and

280 nitrated mono-unsaturated oxidation products were fitted during the MCGA optimization and determined to have saturation

mass concentrations C^* of 1560 and 292 µg/m^3 at 298 K, respectively. During peak growth, 27 % of oxidation products still

contain a double bond in this model run, almost all of which are nitrated and present in the oligomer phase. Note that this is

possible because we do not consider the oxidation of unsaturated compounds in the particle phase.

The volatility distributions determined by global optimization can be found in Fig. S5a. The majority of limonene oxidation

285 products in this model run occupies the 4th and 5th volatility bins ($C^* = 100$, 1000 µg/m^3 at 298 K), which are mostly present

in the gas phase under these reaction conditions. In the model, the slow increase in aerosol mass from 20 minutes to 5 hours

of oxidation is due to oligomerization of monomers forming higher molecular weight structures through accretion reactions

in the particle phase (from now on referred to as "oligomers"). According to the model fit, oligomerization occurs at a rate of

1 h^{-1}, hereby slowly removing semi-volatile species in the particle phase from partitioning equilibrium and causing a slow

290 drift of semi-volatiles from the gas phase into the particle phase. At peak growth, most of the organic material in the particle

phase exists in an oligomeric state, cf. Fig. 2b, panel (ii), which explains the lack of initial evaporation caused by an increase

in chamber temperature.

Surprisingly, the SOA yield observed at 5 °C in this study is lower than in experiments performed at 25 °C previously (Boyd

et al., 2017). A potential justification could be temperature dependence of the oligomerization rate constant. In chamber ex-

295 periments, condensation of vapors onto the particles stands in competition with irreversible loss to the chamber walls, which

we assume to be temperature independent. When oligomerization occurs more slowly, oxidation products from the $C^* = 100$

and 1000 µg/m^3 volatility bins are increasingly lost to the walls instead of being incorporated into the particle oligomer phase.

Furthermore, Boyd et al. (2017) observed a lower aerosol mass when forming limonene SOA at 40 °C compared to first form-

ing limonene SOA at 25 °C and then heating to 40 °C. Also here, a possible explanation is the formation of oligomers of

300 semi-volatile vapors: the fractional amount of chemical species from the 100 and 1000 µg/m^3 volatility bins that partitions

into the particle phase is much smaller at 40 °C and hence prevents mass accumulation through oligomerization.

The slow decay of aerosol mass between 6 and 24 hours of the experiment is attributed in the model to a slow unimolecular decay of oligomeric material with a rate constant of $0.04\ \mathrm{h}^{-1}$, followed by evaporation of monomers at elevated temperatures, and subsequent irreversible deposition of vapors onto the chamber walls. The observed decomposition rate is slightly slower

305   than the rate of $0.06 - 0.2\ \mathrm{h}^{-1}$ reported by D'Ambro et al. (2018) for SOA formed from ozonolysis of α-pinene. Following Le Chatelier's principle, removal of monomers from the equilibrium causes a constant drift of organic matter from oligomeric to monomeric state. Since the volatility of the monomeric subunit is retained in the model (for details see oligomerization mechanism in Fig. S3), this process is faster for monomers that have higher volatilities because they partition into the gas phase more quickly and readily, causing an enrichment of low-volatility monomeric subunits in the particle phase. The (meta-

310   )stability of organic material in the particle phase can hence be attributed not only to the stability of the oligomer bond, but also the volatility of the monomeric building blocks at this temperature.

Monomers and dimers are removed from the system by loss to the chamber walls, which is the main driver of loss of organic mass. The loss coefficient of gas-phase molecules to the chamber wall is determined to be 3.3×10^{-7}. This number is interpreted as a gas-wall accommodation coefficient of molecules colliding with the chamber wall and is used for all organic

315   molecules independent of their chemical structure. In this study, it is assumed that molecules adsorbed to the chamber walls are irreversibly lost for the time scale of the experiment. This can be explained by slow diffusion of molecules into the inner layer of the Teflon wall (Huang et al., 2018). In the geometry of the GTEC and for $250\ \mathrm{g/mol}$ molecules at 298 K, a loss coefficient of 2.8×10^{-7} corresponds to a loss rate of $0.12\ \mathrm{h}^{-1}$ or a gas-wall equilibration timescale τ_{gwe} of 3.0×10^{4} s, respectively. This number falls in-between values previously reported in the literature. Krechmer et al. (2016) as well as Yeh and Ziemann (2015)

320   reported a τ_{gwe} around 1×10^{3} s in their Teflon chamber, whereas gas-wall equilibration timescales measured in the CalTech chamber typically range from 3×10^{4} s and 5×10^{5} s, depending on the chemical identity of the investigated substance (Loza et al., 2010; Shiraiwa et al., 2013; Zhang et al., 2015a).

3.2 Pure α-pinene oxidation (APN)

3.2.1 Experimental observations (APN)

325   Fig. 3a shows the aerosol mass during the corresponding experiment of α-pinene oxidation with NO$_3$, here referred to as "APN" experiment. Similar to the LIM experiment described above, oxidation at 5 °C initially causes a fast increase in aerosol mass (black open markers), however, peak aerosol mass is reached already after 3 hours of oxidation at $109\ \mathrm{\mu g/m^3}$. Due to the larger amount of injected precursor, SOA yield is at 25.2 % significantly lower than observed in the limonene oxidation experiment (Table 2). However, this yield appears to be larger than previously reported for the oxidation of α-pinene with

330   NO$_3$: Hallquist et al. (1999) measured a 7 % yield (corresponding to $52.9\ \mathrm{\mu g/m^3}$ organic aerosol) at 15 °C. Nah et al. (2016) measured a yield of 3.6 % (corresponding to $2.4\ \mathrm{\mu g/m^3}$ organic aerosol) at room temperature. Fry et al. (2014) reported no significant aerosol growth at room temperature. This is indicative of the low temperature employed in the experiments having a significant impact on SOA yield.
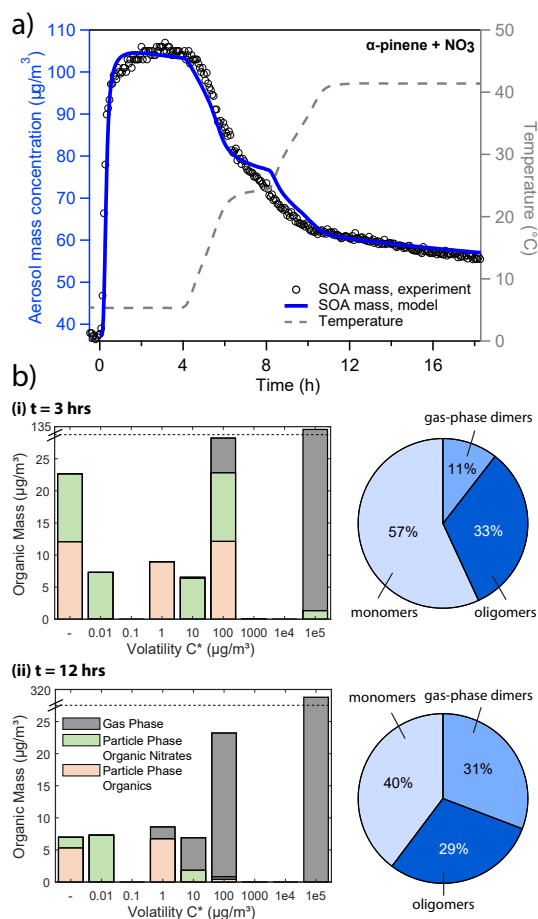
Figure 3. (a) Comparison of experimental and modelling results of aerosol mass for oxidation of α-pinene with NO_3. Open black markers are experimental aerosol masses obtained using an SMPS. The blue solid line represents a model result and the grey dashed line corresponds to the experimental temperature profile. (b) Analysis of the occupation of volatility bins of all products (bar plot) and oligomerization state of particle-phase products (pie chart) in the model (i) 3 hours and (ii) 12 hours after the beginning of the experiment. Shadings in the bar plot denote where molecules of a certain volatility bin reside: gas phase (grey) or particle phase (colored). Products in the particle phase are further distinguished as ON (green) and non-nitrated organics (orange).

After about 4 hours of total experiment time, the temperature set point of the chamber enclosure is increased to 25 °C,
335 leading to a sharp and significant evaporation of organic material from aerosol particles. When the new temperature plateau is reached after 7 hours, aerosol mass has decreased to 80 μg/m³. Since evaporation has hardly slowed down by that time, heating to the new temperature set point of 42 °C is initiated after 8 hours of experiment time (i.e., without long waiting time at the 25 °C temperature plateau) to avoid losing too much volatile aerosol mass from evaporation. After a chamber temperature of 42 °C is reached after 10 hours, evaporation slows down considerably and continues at a slow rate until the end of the

340 experiment, where a minimum aerosol mass of 57 μg/m^3 is observed. With a seed mass of 37.3 μg/m^3, this corresponds to a retained organic aerosol mass of about 20 μg/m^3 (cf. Table 2).

3.2.2 Kinetic modelling results (APN)

The kinetic model (blue solid line in Fig. 3a) shows a reasonable correlation to the experimental data. The detailed model analysis in Fig. 3b reveals that at peak growth, the aerosol is composed of about 57 % of monomers and an aggregate 43 % of

345 higher molecular weight structures, i.e., 33 % oligomers and 11 % gas-phase dimers (Fig. 3b (i)). Upon increase in chamber temperature, the gas-phase dimer content increases considerably from 11 % to 31 % (panel ii) due to evaporation of monomers in volatility bins $C^* = 1 - 100$ μg/m^3 and decomposition of oligomers. Hence, the slower evaporation of organic material toward the end of the experiment can be attributed to the fact that the remaining organic aerosol is only comprised of gas-phase dimers ($C^* = 0.01$ μg/m^3), low-volatile monomers ($C^* = 0.01 - 1$ μg/m^3 volatility bins) and oligomers composed of

350 low-volatile monomer building blocks (Fig. 3b (ii)). The volatility distributions of the monomers produced from gas-phase chemistry (Fig. S5b) reveal that a large fraction of nitrated monomers occupy the highest volatility bin and does not partition into the particle phase. Since the majority of the oxidation products of the reaction of α-pinene with NO$_3$ are nitrated organics, this could explain the lower SOA yield compared to the reaction of α-pinene with O$_3$ or OH (Hoffmann et al., 1997; Griffin et al., 1999; Ng et al., 2007; Eddingsaas et al., 2012; Nah et al., 2017) since non-nitrated monomers also occupy lower volatility

355 bins in this specific global optimization result.

Compared to the LIM experiment, peak aerosol mass is reached more quickly in the APN experiment. In the model solution, this is due to the determined oligomer formation rate being comparatively high at 17.4 h^{-1}, which is an order of magnitude faster than determined for the LIM experiment. On the other hand, the oligomer decomposition rate is determined to be 3.3 h^{-1}, which is two orders of magnitude quicker than that determined for the LIM experiment and one order of magnitude quicker

360 than the rates reported by D'Ambro et al. (2018) for α-pinene ozonolysis. This leads to an overall lower, more quickly formed, but labile oligomer content for the APN experiment. The higher gas-phase dimer concentration can be explained by the higher initial precursor concentration used in the APN experiment that leads to a more pronounced RO$_2$ + RO$_2$ gas-phase chemistry.

Evaporation in the model slows down once the 25 °C temperature plateau is reached and picks up again after temperature is raised. This behavior is not observed in the experiment, where the evaporation rate remains almost constant, irrespective of

365 chamber temperature between hours 5 and 9 of the experiment. The behavior cannot be reproduced in any model run and the implications of these findings will be discussed in Sect. 3.4.3.

3.3 Simultaneous and sequential oxidation experiments (MIX and SEQ)

In addition to oxidation experiments with single precursors, experiments are performed where α-pinene and limonene are oxidized simultaneously (MIX) or in sequence (SEQ) to investigate whether their co-existence affects growth or evaporation

370 of SOA. In Figs. 4a (MIX) and 4b (SEQ), aerosol mass is displayed for these two scenarios alongside kinetic modelling results. The experiments are set up in a way that the produced aerosol mass is comparable in magnitude to the pure precursor
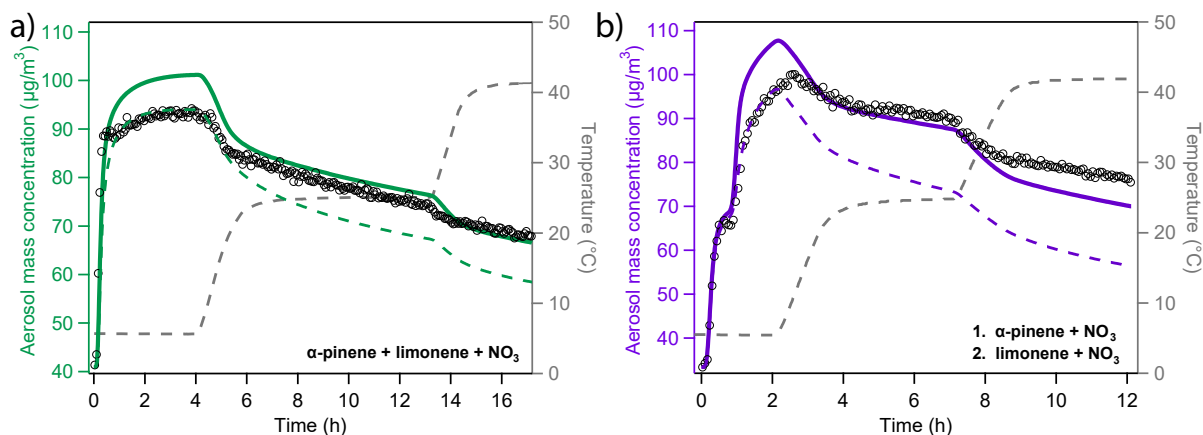
Figure 4. Overview of experimental and modelling results of aerosol mass for experiments with mixed monoterpene precursors. The experiments in the two panels differ in the way the precursors were added: (a) simultaneous oxidation of a mixture of α-pinene and limonene, (b) sequential oxidation of firstly α-pinene and secondly limonene with NO_3. Open black markers are experimental aerosol mass obtained using an SMPS. The colored solid and dashed lines represent model results from two different fits to the experimental data. The grey dashed line indicates the experimental temperature profile.

experiments and both precursors contribute to the produced mass in equal parts. Table 2 lists the experimental SOA yields along with injected precursor amounts.

3.3.1 Experimental observations (MIX and SEQ)

375 In the MIX experiment (Fig. 4a), most of the initial increase in aerosol mass (black open markers) is rapid and peak growth is reached after about 3 hours, comparable to the pure α-pinene oxidation experiment. The evaporation pattern upon chamber heating shows a less pronounced decrease in particle mass compared to the APN experiment, but is more pronounced than observed in the LIM experiment. Overall, the mass loss during the 5 °C to 25 °C evaporation step is more pronounced than mass loss during the 25 °C to 42 °C step.

380 In the SEQ experiment (Fig. 4b), initial growth of α-pinene SOA onto the inorganic seed particles is rapid. After subsequent injection of limonene precursor, the second increase in aerosol mass is more gradual, as would be expected from the pure LIM experiment. The evaporation pattern in the SEQ experiment is less pronounced than the one of the MIX experiment during the 5 °C to 25 °C temperature increase and equally marginal from 25 °C to 42 °C.

3.3.2 Kinetic modelling results (MIX and SEQ)

385 The model result of the best fit modelling scenario (solid green and purple lines) lacks in correlation to the experimental data for both, MIX, and SEQ experiments. Strikingly, the mass at peak aerosol growth is overestimated by the model in both scenarios. Furthermore, initial evaporation is overestimated such that aerosol mass in the middle and late stages of the experiments

agrees between model and experiment. Towards the end of the experiment, evaporation is further overestimated in the SEQ experiment, such that predicted aerosol mass becomes lower than the experimentally observed mass.

390   The best fit modelling result is generated from optimization to aerosol mass and pON/OA data from experimental data sets LIM, APN, and SEQ; experiment MIX is left out for cross-validation. Furthermore, pure precursor experiments are each weighted twice as high as the SEQ experiment. pON/OA data are weighted by a factor of 4 less than aerosol mass data. The model optimization is hence intentionally biased towards aerosol mass of the pure precursor experiments. The premise of this decision is to investigate the potentially non-linear effects of mixing precursors, which cannot be accomplished if the pure

395   precursor experiments are not accurately represented in the first place. We note that fitting to all four data sets with equal weighting coefficients does not yield a subjectively better optimization result and only shifts insufficient model-experiment correlation to the pure precursor experiments APN and LIM.

Figs. 4a and 4b also show a different modelling scenario that is obtained by only optimizing to the APN and LIM experiments (dashed green and purple lines), with experiments MIX and SEQ left out for cross-validation. This scenario shows agreement

400   between model and mixed precursor experiments during peak growth, but significantly underestimates aerosol mass after the first increase in chamber temperature. If applied to all data sets, this fit scores worse in the least-squares residue between model and experiment (Eq. 4) than the best fit scenario described above, however, overestimation of evaporation in the mixed precursor experiment is a common theme between modelling scenarios that were able to reproduce both the growth and evaporation of the pure precursor experiments. Of note, evaporation is generally more strongly overestimated in the SEQ experiment, where

405   limonene SOA is deposited onto α-pinene SOA that has already formed.

These results are similar to the findings of Boyd et al. (2017), who showed less evaporation of limonene SOA and more evaporation of β-pinene SOA in a SEQ-type experiment (β-pinene SOA condensing on preformed limonene SOA) compared to their MIX-type experiment. The study postulated a core-shell morphology of a limonene SOA core and a β-pinene SOA shell that is sustained due to incomplete mixing, though oligomerization between limonene and β-pinene oxidation products could

410   also play a role. Here, we show in a proof of concept that oligomerization mechanics alone cannot explain the evaporation of monoterpene SOA mixtures. In the following, we will take a closer look at further possible explanations.

3.4   Deviation between model and experiment

We can conclude that while peak aerosol mass can be reconciled between the four simulated experiments with the kinetic model, the evaporation pattern in experiments MIX and SEQ cannot be brought fully into agreement with the pure precursor

415   experiments LIM and APN. Hence, the kinetic model must lack a process that leads to resistance in evaporation in the mixed precursor scenarios compared to the pure precursor experiments. Possible mechanisms introducing such non-linearity include:

1. Non-linear gas-phase chemistry

2. Augmented particle-phase oligomerization chemistry

3. Mass transfer limitations

420   In general, none of these points can be fully excluded based on the results presented in this manuscript. However, in the following, we will go through the obtained evidence and evaluate these points to make an informed guess on how likely they are to affect aerosol formation and evaporation.

3.4.1 Gas-phase chemistry

Non-linear effects in gas-phase chemistry branching ratios could lead to a mixture of oxidation products that is more readily
425   oxidized or dimerized and hence would show a reduced evaporation rate upon increase in chamber temperature. One possible mechanism for this is an increased yield of gas-phase dimers due to bimolecular reaction of two RO_2 radicals from different precursors, forming hetero-dimers of oxidation products. Formation of hetero-dimers is considered in the model, however, the branching ratio is assumed to be similar for limonene- and α-pinene-derived molecules and hence self-reactions are of the same speed as cross-reactions. Berndt et al. (2018) showed that cross-reactions of two different α-pinene-derived RO_2 radicals
430   can be faster than the respective self-reaction rates. Such an effect would cause a higher dimer fraction in the product spectrum, which in turn would lead to reduced evaporation of SOA from precursor mixtures due to overall lower volatility. Since in precursor mixtures the number of RO_2 radicals is diversified, more cross-reactions will occur naturally, which would lead to more gas-phase dimers and in turn explain the slower evaporation in the MIX experiment. The SEQ experiment, however, also shows slow evaporation compared to the pure precursor experiment. Since oxidation occurred separately and cross-reactions
435   are not enhanced by diversification of RO_2 radicals, formation of hetero-dimers in the gas phase cannot be the cause for reduced product volatility in the SEQ experiment.

3.4.2 Oligomerization

Augmented oligomerization in the particle phase is a possible explanation of reduced evaporation rates in case mixtures of oxidation products from different precursors oligomerize more readily together than the pure components in isolation. Unlike
440   the gas-phase chemistry scenarios described above, these effects could be observed in both MIX and SEQ experiments since particle-phase oligomerization may occur retroactively after the second oxidation step in the sequential oxidation experiment. Moreover, oligomerization of already low-volatile products would not alter SOA yields as strongly as gas-phase chemical effects would, but could have a pronounced influence on evaporation rates.

   In general, an augmentation effect leading to a higher oligomerization degree in mixtures could be achieved if the hetero-
445   oligomers were formed more efficiently than a linear combination of formation rates of both homo-oligomers. A similar effect would be achieved when oxidation products of one of the two precursors were such efficient oligomer-formers that they would cause the oxidation products of the other precursors to oligomerize more readily and pull them into the oligomer phase. Therefore, during development of the model, we tested an implementation of the oligomerization scheme where formation of hetero-oligomers occurs at a combined rate using their logarithmic mean value, but first-order decomposition rates remain unaffected
450   by the precursor type. The model solution exhibited a large discrepancy in oligomerization rates of a few orders of magnitudes, with limonene oxidation products oligomerizing quickly and readily and α-pinene oxidation products hardly oligomerizing in isolation. As a result, mixtures of oxidation products still oligomerized significantly, driven by the high individual oligomer

formation rate of limonene oxidation products. Equilibrium oligomerization degree is governed by both oligomer formation and decomposition rates, but is also naturally capped to a value of 100 %. Hence, in conclusion, mixing a strong oligomer

455 former that reaches this cap in isolation with a weak oligomer former can lead to a higher combined oligomerization degree of the mixture. However, this pure theoretical result seems unphysical as it requires a very high oligomerization degree of pure limonene SOA and a very small degree of oligomerization in pure α-pinene SOA, which has not been observed in experimental studies (Faxon et al., 2018; Takeuchi and Ng, 2019).

3.4.3 Mass transfer limitations

460 Increased mass transfer limitations caused by high viscosity can cause a reduction of volatilization. This is due to surface concentrations of the evaporating components being depleted when the mixing time scale in the particle is longer than the evaporation time scale. Mass transfer limitation is not treated in the model runs previously shown in this study. Instead, a well-mixed bulk phase is assumed and any resistance in evaporation is explained with oligomerization reactions. The slow evaporation of limonene SOA is hence solely caused by significant oligomerization in the model runs previously presented,

465 but could also be caused by mass transfer limitations induced by a high bulk-phase viscosity, especially if a high fraction of particle-phase oligomers would have formed that depresses mobility of molecules in the condensed phase (Baltensperger et al., 2005; D'Ambro et al., 2018). Hence, limonene SOA might exhibit a more viscous phase state than α-pinene SOA. The high viscosity caused by limonene oxidation products might in turn affect evaporation in the mixed precursor experiments and cause the observed non-linear effects. In a first approximation, viscosities of mixtures can be assumed to be a linear combination of

470 the individual viscosities and follow a logarithmic mixing rule (Gervasi et al., 2019). This entails that the change in the rate of mass transport between pure compounds and their mixtures can reach orders of magnitudes. This would be in line with volatilization rates observed in the mixed precursor experiments being more similar to the pure LIM experiment, which was observed in this and a previous study (Boyd et al., 2017). Notably, while evaporation steps immediately following a change in chamber temperature are overall similar between the MIX and SEQ experiments, the slope of the aerosol mass versus time

475 curve is steeper in the MIX experiments. This might suggest that in the SEQ experiment, limonene SOA might be covering the preformed α-pinene oxidation products in a core-shell morphology and thus hampering their volatilization.

To test the effect of impeded bulk diffusivity on the evaporation of SOA, we perform a sensitivity study in which we increase viscosity in the model to evaluate whether the evaporation rates in the MIX experiment can be brought into agreement with observations. We use the alternative fitting scenario shown in Fig. 4 (dashed lines) and raise the viscosity in the simulation to

480 2×10^6, 2×10^7, and 2×10^8 Pas, respectively, in three separate model runs (Fig. 5). These viscosities are in the typical range for SOA under dry conditions and fall into the semi-solid phase state region (Koop et al., 2011; Shiraiwa et al., 2011; Abramson et al., 2013; Zhang et al., 2015b; Grayson et al., 2016; Gervasi et al., 2019). Using the Stokes-Einstein relation (Einstein, 1905) and an effective molecular radius of 2 nm, these viscosities correspond to bulk diffusion coefficients of 5×10^{-16} to 5×10^{-18} cm^2/s at 298 K. The effective radius is approximated from geometric considerations assuming spherical molecular

485 shape, a molar mass of 250 g/mol and density of 1.55 g/cm^3. The temperature dependence of this diffusion coefficient is
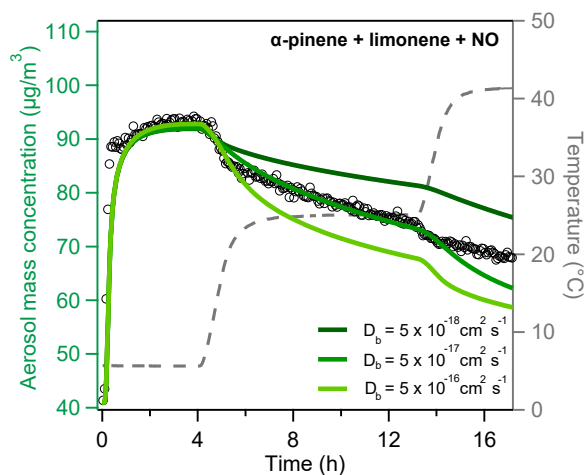
Figure 5. Influence of viscosity on model simulation results based on the alternative fitting scenario and the MIX experiment. Model simulations were performed at different diffusivity coefficients $5 \times 10^{-18} - 5 \times 10^{-16} \ \mathrm{cm^2/s}$, corresponding to bulk viscosities of $2 \times 10^6 - 2 \times 10^8$ Pas according to the Stokes-Einstein relation, Eq. 5.

approximated with a constant activation enthalpy of diffusion $\Delta H_{\mathrm{dif}} = 50 \ \mathrm{kJ/mol}$ according to Eq. 5.

$$D_{\mathrm{b}}(T) = D_{\mathrm{b}}(298 \ \mathrm{K}) \cdot \exp \frac{-\Delta H_{\mathrm{dif}}}{R \left(\frac{1}{T} - \frac{1}{298} \right)} \tag{5}$$

Fig. 5 shows that in the selected viscosity range, the model output is quite sensitive to changes in bulk diffusivity. Evaporation is almost unimpeded in the highest diffusion case, but considerably slowed at the lowest simulated diffusivity. At a bulk

490   diffusion coefficient of $5 \times 10^{-17} \ \mathrm{cm^2/s}$, the correlation with the evaporation pattern in the MIX experiment is much improved. This model result insinuates that the co-presence of limonene SOA and α-pinene SOA might strongly reduce the mobility of α-pinene oxidation products so that the fast evaporation of α-pinene oxidation products observed in the pure α-pinene oxidation experiment does not take place. The outcome of this sensitivity study has to be treated with caution since slow diffusion of limonene oxidation products also causes a change in the simulation outcome for the pure limonene experiment,

495   which the employed parameter set is based on. With this parameter set, the slow evaporation of limonene SOA in the model is purely attributed to oligomer formation. The sensitivity study hence suggests that the high oligomerization degree observed for limonene SOA in the previous best fit solutions might be overestimated. In fact, a particularly high oligomer content was not observed for limonene SOA from oxidation with NO_3 in measurements using FIGAERO-CIMS (Faxon et al., 2018). Distinction of these two effects (oligomerization vs. mass transfer limitation) could be possible with the model and the MCGA,

500   but is not attempted in this study due to the prohibitive computational cost of model calculations at low diffusivities and will be subject of future studies.

Taken together, it is possible that increased mass transfer limitation led to the observed reduced evaporation rates of the SOA mixtures as postulated in Boyd et al. (2017). However, there are still large uncertainties and a high computational expense associated with a model treatment of highly viscous SOA systems. While frameworks for the determination of viscosity of

505 mixtures have recently been developed (Gervasi et al., 2019), these rely on structural information about individual compounds. Furthermore, while the Stokes-Einstein relation seems to hold for similar systems at viscosities of up to 10^4 Pas (Ullmann et al., 2019), it is not clear whether it also holds for viscosities of 10^7 Pas derived in this study (Evoy et al., 2019).

Additionally, treatment of slow particle-phase diffusion requires many model layers to describe the steep concentrations gradients arising at the particle surface upon evaporation. In combination with the multitude of tracked species in the particle
510 phase, computational costs quickly reach unfeasible ranges. Ideally, the spatial resolution model layers would have to be generated upon model runtime by an algorithm that detects steep concentration gradients. This detailed description will be presented in a forthcoming publication.

3.5 Organic nitrate fractions

In this study, the organic nitrate fraction (pON/OA) is presented as ratio of the total mass concentration of particulate ON
515 (which includes the organic part and nitrate part of the ON compounds) to the total mass concentration of organic aerosol (which includes both ON and non-nitrated organics) (Takeuchi and Ng, 2019). It can be inferred from AMS data using Eq. 6. In this formula, it is assumed that all organic aerosol mass is found in the organic and nitrate signal of the AMS (AMS_{ORG} and AMS_{NO3}) and all AMS nitrate is ON. When MW_{pON} is the average molar mass of the ON (i.e., 250 g/mol in this study) and MW_{NO_3} the molar mass of the nitrate group (i.e., 62 g/mol), the pON mass can be determined by scaling the AMS signal with
520 the ratio of these molar masses.

$$\frac{\text{pON}}{\text{OA}} = \frac{AMS_{\text{NO3}} \cdot \frac{MW_{\text{pON}}}{MW_{\text{NO3}}}}{AMS_{\text{NO3}} + AMS_{\text{ORG}}} \approx \frac{4.03}{1 + \frac{AMS_{\text{ORG}}}{AMS_{\text{NO3}}}} \tag{6}$$

Fig. 6 depicts measured and modelled values for pON/OA for all four experiments. Panel a shows that in the LIM experiment, pON/OA is high, with a mass ratio of about 0.8 in the particle phase, and only slightly increases over time, which is reproduced in the model. Note that the average molar mass of ON might change during the experiment, e.g., by evaporation of lower
525 molecular weight components, which is not considered in our calculation. In the model, the slow evaporation of limonene SOA is caused by oligomer decomposition followed by evaporation of volatile monomers. The fact that nitrate groups are rather evenly distributed across monomers from the predominantly evaporating volatility bins is reflected in the constant pON/OA returned by the model. We note that this result gives no evidence that decomposition rates of oligomers consisting of nitrated or non-nitrated monomeric building blocks might differ and we use the same oligomer decomposition rate irrespective of nitration
530 state of the respective product bin. Panel b shows pON/OA in the APN experiment. The initial nitrate content is lower than in the LIM experiment with a value of about 0.45. During the first temperature increase in the APN experiment, ON content increases with the reduction in organic mass, indicating predominant evaporation of non-nitrated oxidation products. During the second evaporation step, ON content decreases, indicating predominant evaporation of nitrated oxidation product. The best fit model run (solid blue line) captures the overall magnitude of the ON content, but lacks the time dependence of a reduction
535 followed by an increase in pON/OA. This is probably due to the model parameter optimization being stuck in a local minimum and the relatively low weighting coefficients assigned to the pON/OA data sets in this study. pON/OA data were weighted by a factor of 4 less than aerosol mass data in this study.
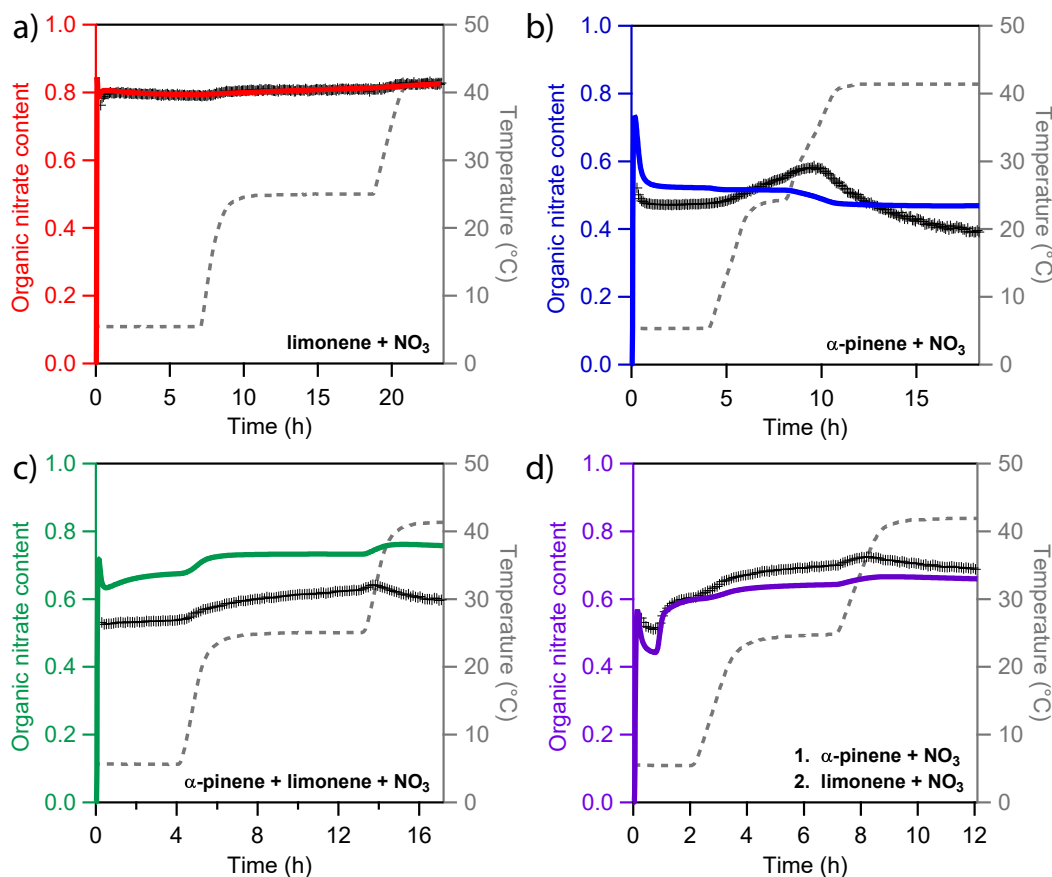
Figure 6. Experimental and modelling results of particulate organic nitrate content (pON/OA) for four different types of chamber-generated SOA. (a) only limonene, (b) only α-pinene, (c) a mixture of α-pinene and limonene and (d) sequential oxidation of firstly α-pinene and secondly limonene. Cross markers are experimental nitration degrees inferred using a High Resolution Time-of-Flight Aerosol Mass Spectrometer (HR-ToF-AMS). The colored solid lines represent results of the kinetic model. The grey dashed line indicates the experimental temperature profile.

The measured and simulated ON contents for the experiments with multiple precursors are shown in panels c and d of Fig. 6 for the MIX and SEQ experiment, respectively. While both experiments use approximately the same concentrations of α-pinene and limonene, the measured pON/OA are slightly different. Simultaneous oxidation (MIX) leads to an initial pON/OA of 0.53, which is surprisingly low and closer to the value measured for pure α-pinene SOA. Sequential oxidation (SEQ) leads to an initial pON/OA of 0.52 after α-pinene oxidation, and increases to 0.6 after oxidation of limonene has concluded. This value in the SEQ experiment is closer to the expected value when assuming linear additivity of ON content. The unexpectedly low ON content in the MIX experiment points towards non-linear effects in chemistry that are not captured by the model. The time and temperature dependence of the ON fraction is qualitatively similar for both experiments and overall captured by the

model. Predominant evaporation of α-pinene oxidation products, which are the more-volatile and less-nitrated components of the mixture, leads to an overall increase of pON/OA.

A notable observation from modelling is that dimers from the gas-phase reaction of RO_2 + RO_2 are mainly ON because most RO_2 radicals originate from the reaction of alkene with NO_3 and are hence nitrated. This is especially significant for the
550 α-pinene + NO_3 reaction system since the high momentary RO_2 radical concentrations in these experiments lead to a high estimated contribution of gas-phase dimers to aerosol mass of 11 % at peak growth and close to 31 % after heating to 42 °C (cf. Fig. 3).

In summary, the experimental and modelling results in this study confirm previous studies and report a high efficiency of nitration in the reaction of monoterpenes with NO_3, with a nitrated SOA fraction larger than 50 % under most experimental
555 conditions studies (Ng et al., 2017, and references therein). Limonene SOA shows overall higher nitration degrees than α-pinene SOA, which can be understood by the higher number of double bonds of the VOC precursor compound itself and hence more possibilities to introduce a nitrate group during oxidation. An increase in temperature from 5 °C to 25 °C leads to an increase in ON content of the SOA in all observed systems, which can be explained by the slightly elevated nitration degree in the dimer fraction and hence less volatile fraction of the organic aerosol. By heating above 25 °C, pON/OA is in general
560 slightly reduced. A potential reason for this might be accelerated thermal decomposition of ON.

4 Conclusions and Outlook

In this study, an inverse modelling approach is utilized alongside laboratory chamber experiments to gain insights into the molecular-level processes which occur during the formation and evaporation of SOA from the oxidation of α-pinene, limonene, and mixtures of both precursors with NO_3. We find α-pinene SOA to form and evaporate rather quickly and limonene SOA
565 to form and evaporate more slowly. Both SOA types, however, show retardation in evaporation compared to instantaneous equilibration, which can be explained by the presence of particle-phase oligomers. The oxidation products of both SOA types are found to be heavily nitrated. A mixed and a sequential oxidation of both precursors shows the expected linear additivity of SOA yields, but a non-linear reduction in evaporation behavior, which could not be explained without diffusion limitations in the particle phase. These results highlight the significance of NO_3 as oxidant in SOA formation and the importance of ON as
570 products of monoterpene oxidation. This study finds evidence for non-equilibrium partitioning caused by slow particle-phase chemistry and slow diffusion, which is currently not considered in global models and may lead to underestimation of SOA persistence and hence underestimated global SOA burdens in these models.

The modelling approach applied in this study comprises a combination of the kinetic multi-layer model based on KM-GAP (Shiraiwa et al., 2012) with the automated global optimization suite MCGA (Berkemeier et al., 2017) and details the
575 full chemistry and physics of SOA particle growth and shrinkage. The underlying SOA formation and evaporation mechanism uses a simplified and lumped version of the Master Chemical Mechanism (MCM; Jenkin et al., 2003; Saunders et al., 2003; Berkemeier et al., 2016), extends it with a reversible particle-phase oligomerization and gas-phase dimerization scheme, and treats gas-particle partitioning with a volatility basis set approach (Donahue et al., 2006, 2011) for each product bin. This

study focuses on NO$_3$ oxidation of monoterpenes and their mixtures, but the model framework can be ported to other chemical

580   systems. The depth resolution capabilities of the multi-layer model allow for a sensitivity study of the influence of particle

phase state on the evaporation of these particles. A full treatment of composition-dependent, depth-resolved viscosity as global

optimization parameter is ultimately needed to disentangle the interactions of particle-phase diffusion and particle-phase chem-

istry. Due to the computational expense of finely-resolved computational layers and the general uncertainty in the physical and

chemical parameters, this will be subject of follow-up studies. In such studies, offline analysis of the oligomerization degree of

585   SOA material can help to constrain oligomerization and oligomer decomposition rates and thermodynamic models can be used

to provide estimates for composition dependence of viscosities and diffusivities (DeRieux et al., 2018; Gervasi et al., 2019).

In general, the model parameters that are returned by the inverse modelling approach applied in this work must be evaluated

in the context of the model and experimental data that are employed. With a simplified multi-parameter model and experimental

data sets that are aggregate observables and subject to uncertainty, the concept of a single global minimum and multiple local

590   minima on the optimization hypersurface can become blurred and several extended areas on the optimization hypersurface can

exhibit a minimal function value. This effect is enhanced when model parameters behave non-orthogonally, i.e., one parameter

can by expressed to some extent by another one (or combinations of others). The existence of numerous and extended minima

on the optimization hypersurface makes the process of finding an optimal parameter set computationally expensive. For exam-

ple, repeated execution of an automated fitting algorithm can help to assess the flexibility of an underdetermined system. Fig.

595   S5 includes an estimation of the uncertainty in volatility distributions obtained in this study. The error bars in Fig. S5 are stan-

dard deviations of individual re-fits of volatility distributions and hence quantify the uniqueness (or lack thereof) of the fitted

volatility distributions. Beyond the technical intricacies of the parameter optimization process, the uniqueness of the obtained

parameter set can be enhanced by inclusion of more experimental data at different conditions or by a priori determination of

model parameters such as measurements of volatility distributions, oligomerization degrees or particle viscosities.

600   The modelling suite presented here constitutes a step forward in the computational, data-driven evaluation of SOA formation

with kinetic models. In this work, only a small set of laboratory chamber data is utilized for optimization as proof of concept. We

postulate that, by reconciling and cross-comparing large sets of experimental data, we will be able to significantly enhance our

understanding of SOA and close the gap between our expanding theoretical knowledge about the detailed gas-phase chemistry,

gas-particle partitioning, particle phase state of SOA, and the application of this knowledge in chemical transport models.

605   *Data availability.* Data are available upon request from the corresponding authors (t.berkemeier@mpic.de, ng@chbe.gatech.edu).

Author contributions. TB and NN designed research. TB, MT, and GE conducted experiments. TB developed the model code and performed

simulations. TB, MT, and NN analyzed data. TB prepared the manuscript with contributions from all co-authors.

Competing interests. The authors declare no conflict of interest.

Acknowledgements. This work was supported by NSF CAREER AGS-1555034. T. Berkemeier acknowledged support by the Eckert Post-
610   doctoral Fellowship from the School of Chemical and Biomolecular Engineering at Georgia Institute of Technology.

References

Abramson, E., Imre, D., Beranek, J., Wilson, J. M., and Zelenyuk, A.: Experimental determination of chemical diffusion within secondary organic aerosol particles, Phys. Chem. Chem. Phys., 15, 2983–2991, https://doi.org/10.1039/c2cp44013j, 2013.

Baltensperger, U., Kalberer, M., Dommen, J., Paulsen, D., Alfarra, M. R., Coe, H., Fisseha, R., Gascho, A., Gysel, M., Nyeki, S., Sax, M., Steinbacher, M., Prevot, A. S. H., Sjögren, S., Weingartner, E., and Zenobi, R.: Secondary organic aerosols from anthropogenic and biogenic precursors, Faraday Discuss., 130, 265–278, https://doi.org/10.1039/B417367H, 2005.

Berkemeier, T., Huisman, A. J., Ammann, M., Shiraiwa, M., Koop, T., and Pöschl, U.: Kinetic regimes and limiting cases of gas uptake and heterogeneous reactions in atmospheric aerosols and clouds: a general classification scheme, Atmos. Chem. Phys., 13, 6663–6686, https://doi.org/10.5194/acp-13-6663-2013, 2013.

Berkemeier, T., Ammann, M., Mentel, T. F., Pöschl, U., and Shiraiwa, M.: Organic Nitrate Contribution to New Particle Formation and Growth in Secondary Organic Aerosols from α-Pinene Ozonolysis, Environ. Sci. Technol., 50, 6334–6342, https://doi.org/10.1021/acs.est.6b00961, 2016.

Berkemeier, T., Ammann, M., Krieger, U. K., Peter, T., Spichtinger, P., Pöschl, U., Shiraiwa, M., and Huisman, A. J.: Technical note: Monte Carlo genetic algorithm (MCGA) for model analysis of multiphase chemical kinetics to determine transport and reaction rate coefficients using multiple experimental data sets, Atmos. Chem. Phys., 17, 8021–8029, https://doi.org/10.5194/acp-17-8021-2017, 2017.

Berndt, T., Mentler, B., Scholz, W., Fischer, L., Herrmann, H., Kulmala, M., and Hansel, A.: Accretion Product Formation from Ozonolysis and OH Radical Reaction of α-Pinene: Mechanistic Insight and the Influence of Isoprene and Ethylene, Environ. Sci. Technol., 52, 11 069–11 077, https://doi.org/10.1021/acs.est.8b02210, 2018.

Boyd, C. M., Sanchez, J., Xu, L., Eugene, A. J., Nah, T., Tuet, W. Y., Guzman, M. I., and Ng, N. L.: Secondary organic aerosol formation from the beta-pinene+NO3 system: effect of humidity and peroxy radical fate, Atmos. Chem. Phys., 15, 7497–7522, https://doi.org/10.5194/acp-15-7497-2015, 2015.

Boyd, C. M., Nah, T., Xu, L., Berkemeier, T., and Ng, N. L.: Secondary Organic Aerosol (SOA) from Nitrate Radical Oxidation of Monoterpenes: Effects of Temperature, Dilution, and Humidity on Aerosol Formation, Mixing, and Evaporation, Environ. Sci. Technol., 51, 7831–7841, https://doi.org/10.1021/acs.est.7b01460, 2017.

Cappa, C. D. and Wilson, K. R.: Evolution of organic aerosol mass spectra upon heating: implications for OA phase and partitioning behavior, Atmos. Chem. Phys., 11, 1895–1911, https://doi.org/10.5194/acp-11-1895-2011, 2011.

Claflin, M. S. and Ziemann, P. J.: Identification and Quantitation of Aerosol Products of the Reaction of β-Pinene with NO3 Radicals and Implications for Gas- and Particle-Phase Reaction Mechanisms, J. Phys. Chem. A, 122, 3640–3652, https://doi.org/10.1021/acs.jpca.8b00692, 2018.

DeCarlo, P. F., Kimmel, J. R., Trimborn, A., Northway, M. J., Jayne, J. T., Aiken, A. C., Gonin, M., Fuhrer, K., Horvath, T., Docherty, K. S., Worsnop, D. R., and Jimenez, J. L.: Field-Deployable, High-Resolution, Time-of-Flight Aerosol Mass Spectrometer, Anal. Chem., 78, 8281–8289, https://doi.org/10.1021/ac061249n, 2006.

DeRieux, W. S. W., Li, Y., Lin, P., Laskin, J., Laskin, A., Bertram, A. K., Nizkorodov, S. A., and Shiraiwa, M.: Predicting the glass transition temperature and viscosity of secondary organic material using molecular composition, Atmos. Chem. Phys., 18, 6331–6351, https://doi.org/10.5194/acp-18-6331-2018, 2018.

Donahue, N. M., Robinson, A. L., Stanier, C. O., and Pandis, S. N.: Coupled partitioning, dilution, and chemical aging of semivolatile organics, Environ. Sci. Technol., 40, 2635–2643, https://doi.org/10.1021/es052297c, 2006.

Donahue, N. M., Epstein, S. A., Pandis, S. N., and Robinson, A. L.: A two-dimensional volatility basis set: 1. organic-aerosol mixing thermodynamics, Atmos. Chem. Phys., 11, 3303–3318, https://doi.org/10.5194/acp-11-3303-2011, 2011.

650 Draper, D. C., Myllys, N., Hyttinen, N., Møller, K. H., Kjaergaard, H. G., Fry, J. L., Smith, J. N., and Kurtén, T.: Formation of Highly Oxidized Molecules from NO3 Radical Initiated Oxidation of Δ-3-Carene: A Mechanistic Study, ACS Earth Space Chem., 3, 1460–1470, https://doi.org/10.1021/acsearthspacechem.9b00143, 2019.

D'Ambro, E. L., Schobesberger, S., Zaveri, R. A., Shilling, J. E., Lee, B. H., Lopez-Hilfiker, F. D., Mohr, C., and Thornton, J. A.: Isothermal Evaporation of α-Pinene Ozonolysis SOA: Volatility, Phase State, and Oligomeric Composition, ACS Earth Space Chem., 2, 1058–1067,
655 https://doi.org/10.1021/acsearthspacechem.8b00084, 2018.

Eddingsaas, N. C., Loza, C. L., Yee, L. D., Chan, M., Schilling, K. A., Chhabra, P. S., Seinfeld, J. H., and Wennberg, P. O.: α-pinene photooxidation under controlled chemical conditions - Part 2: SOA yield and composition in low- and high-NOx environments, Atmos. Chem. Phys., 12, 7413–7427, https://doi.org/10.5194/acp-12-7413-2012, 2012.

Einstein, A.: Über die von der molekularkinetischen Theorie der Wärme geforderte Bewegung von in ruhenden Flüssigkeiten suspendierten
660 Teilchen, Ann. Phys., 322, 549–560, https://doi.org/10.1002/andp.19053220806, 1905.

Evoy, E., Maclean, A. M., Rovelli, G., Li, Y., Tsimpidi, A. P., Karydis, V. A., Kamal, S., Lelieveld, J., Shiraiwa, M., Reid, J. P., and Bertram, A. K.: Predictions of diffusion rates of large organic molecules in secondary organic aerosols using the Stokes–Einstein and fractional Stokes–Einstein relations, Atmos. Chem. Phys., 19, 10 073–10 085, https://doi.org/10.5194/acp-19-10073-2019, 2019.

Faxon, C., Hammes, J., Le Breton, M., Pathak, R. K., and Hallquist, M.: Characterization of organic nitrate constituents of secondary organic
665 aerosol (SOA) from nitrate-radical-initiated oxidation of limonene using high-resolution chemical ionization mass spectrometry, Atmos. Chem. Phys., 18, 5467–5481, https://doi.org/10.5194/acp-18-5467-2018, 2018.

Fry, J. L., Kiendler-Scharr, A., Rollins, A. W., Wooldridge, P. J., Brown, S. S., Fuchs, H., Dubé, W., Mensah, A., dal Maso, M., Tillmann, R., Dorn, H. P., Brauers, T., and Cohen, R. C.: Organic nitrate and secondary organic aerosol yield from NO3 oxidation of β-pinene evaluated using a gas-phase kinetics/aerosol partitioning model, Atmos. Chem. Phys., 9, 1431–1449, https://doi.org/10.5194/acp-9-1431-
670 2009, 2009.

Fry, J. L., Kiendler-Scharr, A., Rollins, A. W., Brauers, T., Brown, S. S., Dorn, H. P., Dubé, W. P., Fuchs, H., Mensah, A., Rohrer, F., Tillmann, R., Wahner, A., Wooldridge, P. J., and Cohen, R. C.: SOA from limonene: role of NO3 in its generation and degradation, Atmos. Chem. Phys., 11, 3879–3894, https://doi.org/10.5194/acp-11-3879-2011, 2011.

Fry, J. L., Draper, D. C., Barsanti, K. C., Smith, J. N., Ortega, J., Winkler, P. M., Lawler, M. J., Brown, S. S., Edwards, P. M., Cohen, R. C.,
675 and Lee, L.: Secondary Organic Aerosol Formation and Organic Nitrate Yield from NO3 Oxidation of Biogenic Hydrocarbons, Environ. Sci. Technol., 48, 11 944–11 953, https://doi.org/10.1021/es502204x, 2014.

Fuzzi, S., Andreae, M. O., Huebert, B. J., Kulmala, M., Bond, T. C., Boy, M., Doherty, S. J., Guenther, A., Kanakidou, M., Kawamura, K., Kerminen, V. M., Lohmann, U., Russell, L. M., and Pöschl, U.: Critical assessment of the current state of scientific knowledge, terminology, and research needs concerning the role of organic aerosols in the atmosphere, climate, and global change, Atmos. Chem.
680 Phys., 6, 2017–2038, https://doi.org/10.5194/acp-6-2017-2006, 2006.

Gao, Y., Hall, W. A., and Johnston, M. V.: Molecular Composition of Monoterpene Secondary Organic Aerosol at Low Mass Loading, Environ. Sci. Technol., 44, 7897–7902, https://doi.org/10.1021/es101861k, 2010.

Gatzsche, K., Iinuma, Y., Tilgner, A., Mutzel, A., Berndt, T., and Wolke, R.: Kinetic modeling studies of SOA formation from α-pinene ozonolysis, Atmos. Chem. Phys., 17, 13 187–13 211, https://doi.org/10.5194/acp-17-13187-2017, 2017.

685   Gervasi, N. R., Topping, D. O., and Zuend, A.: A predictive group-contribution model for the viscosity of aqueous organic aerosol, Atmos. Chem. Phys. Discuss., 2019, 1–32, https://doi.org/10.5194/acp-2019-699, 2019.

Grayson, J. W., Zhang, Y., Mutzel, A., Renbaum-Wolff, L., Böge, O., Kamal, S., Herrmann, H., Martin, S. T., and Bertram, A. K.: Effect of varying experimental conditions on the viscosity of α-pinene derived secondary organic material, Atmos. Chem. Phys., 16, 6027–6040, https://doi.org/10.5194/acp-16-6027-2016, 2016.

690   Griffin, R. J., Cocker Iii, D. R., Flagan, R. C., and Seinfeld, J. H.: Organic aerosol formation from the oxidation of biogenic hydrocarbons, J. Geophys. Res. Atmospheres, 104, 3555–3567, https://doi.org/10.1029/1998JD100049, 1999.

Hallquist, M., Wängberg, I., Ljungström, E., Barnes, I., and Becker, K.-H.: Aerosol and Product Yields from NO3 Radical-Initiated Oxidation of Selected Monoterpenes, Environ. Sci. Technol., 33, 553–559, https://doi.org/10.1021/es980292s, 1999.

Hallquist, M., Wenger, J. C., Baltensperger, U., Rudich, Y., Simpson, D., Claeys, M., Dommen, J., Donahue, N. M., George, C., Gold-
695   stein, A. H., Hamilton, J. F., Herrmann, H., Hoffmann, T., Iinuma, Y., Jang, M., Jenkin, M. E., Jimenez, J. L., Kiendler-Scharr, A., Maenhaut, W., McFiggans, G., Mentel, T. F., Monod, A., Prevot, A. S. H., Seinfeld, J. H., Surratt, J. D., Szmigielski, R., and Wildt, J.: The formation, properties and impact of secondary organic aerosol: current and emerging issues, Atmos. Chem. Phys., 9, 5155–5235, https://doi.org/10.5194/acp-9-5155-2009, 2009.

Hoffmann, T., Odum, J. R., Bowman, F., Collins, D., Klockow, D., Flagan, R. C., and Seinfeld, J. H.: Formation of Organic Aerosols from
700   the Oxidation of Biogenic Hydrocarbons, J. Atmos. Chem., 26, 189–222, https://doi.org/10.1023/A:1005734301837, 1997.

Huang, Y., Zhao, R., Charan, S. M., Kenseth, C. M., Zhang, X., and Seinfeld, J. H.: Unified Theory of Vapor–Wall Mass Transport in Teflon-Walled Environmental Chambers, Environ. Sci. Technol., 52, 2134–2142, https://doi.org/10.1021/acs.est.7b05575, 2018.

Jenkin, M. E., Saunders, S. M., Wagner, V., and Pilling, M. J.: Protocol for the development of the Master Chemical Mechanism, MCM v3 (Part B): tropospheric degradation of aromatic volatile organic compounds, Atmos. Chem. Phys., 3, 181–193, https://doi.org/10.5194/acp-
705   3-181-2003, 2003.

Julin, J., Shiraiwa, M., Miles, R. E. H., Reid, J. P., Pöschl, U., and Riipinen, I.: Mass Accommodation of Water: Bridging the Gap Between Molecular Dynamics Simulations and Kinetic Condensation Models, J. Phys. Chem. A, 117, 410–420, https://doi.org/10.1021/jp310594e, 2013.

Kalberer, M., Paulsen, D., Sax, M., Steinbacher, M., Dommen, J., Prevot, A. S. H., Fisseha, R., Weingartner, E., Frankevich, V., Zenobi,
710   R., and Baltensperger, U.: Identification of polymers as major components of atmospheric organic aerosols, Science, 303, 1659–1662, https://doi.org/10.1126/science.1092185, 2004.

Kanakidou, M., Seinfeld, J. H., Pandis, S. N., Barnes, I., Dentener, F. J., Facchini, M. C., Van Dingenen, R., Ervens, B., Nenes, A., Nielsen, C. J., Swietlicki, E., Putaud, J. P., Balkanski, Y., Fuzzi, S., Horth, J., Moortgat, G. K., Winterhalter, R., Myhre, C. E. L., Tsigaridis, K., Vignati, E., Stephanou, E. G., and Wilson, J.: Organic aerosol and global climate modelling: a review, Atmos. Chem. Phys., 5, 1053–1123,
715   https://doi.org/10.5194/acp-5-1053-2005, 2005.

Keywood, M. D., Varutbangkul, V., Bahreini, R., Flagan, R. C., and Seinfeld, J. H.: Secondary organic aerosol formation from the ozonolysis of cycloalkenes and related compounds, Environ. Sci. Technol., 38, 4157–4164, https://doi.org/10.1021/es035363o, 2004.

Koop, T., Bookhold, J., Shiraiwa, M., and Pöschl, U.: Glass transition and phase state of organic compounds: dependency on molecular properties and implications for secondary organic aerosols in the atmosphere, Phys. Chem. Chem. Phys., 13, 19 238–19 255,
720   https://doi.org/10.1039/C1CP22617G, 2011.

Krechmer, J. E., Pagonis, D., Ziemann, P. J., and Jimenez, J. L.: Quantification of Gas-Wall Partitioning in Teflon Environmental Chambers Using Rapid Bursts of Low-Volatility Oxidized Species Generated in Situ, Environ. Sci. Technol., 50, 5757–5765, https://doi.org/10.1021/acs.est.6b00606, 2016.

Kurtén, T., Møller, K. H., Nguyen, T. B., Schwantes, R. H., Misztal, P. K., Su, L., Wennberg, P. O., Fry, J. L., and Kjaergaard, H. G.: Alkoxy Radical Bond Scissions Explain the Anomalously Low Secondary Organic Aerosol and Organonitrate Yields From α-Pinene + NO3, J. Phys. Chem. Lett., 8, 2826–2834, https://doi.org/10.1021/acs.jpclett.7b01038, 2017.

Liebmann, J., Sobanski, N., Schuladen, J., Karu, E., Hellén, H., Hakola, H., Zha, Q., Ehn, M., Riva, M., Heikkinen, L., Williams, J., Fischer, H., Lelieveld, J., and Crowley, J. N.: Alkyl nitrates in the boreal forest: formation via the NO3-, OH- and O3-induced oxidation of biogenic volatile organic compounds and ambient lifetimes, Atmos. Chem. Phys., 19, 10 391–10 403, https://doi.org/10.5194/acp-19-10391-2019, 2019.

Lopez-Hilfiker, F. D., Mohr, C., Ehn, M., Rubach, F., Kleist, E., Wildt, J., Mentel, T. F., Lutz, A., Hallquist, M., Worsnop, D., and Thornton, J. A.: A novel method for online analysis of gas and particle composition: description and evaluation of a Filter Inlet for Gases and AEROsols (FIGAERO), Atmos. Meas. Tech., 7, 983–1001, https://doi.org/10.5194/amt-7-983-2014, 2014.

Loza, C. L., Chan, A. W. H., Galloway, M. M., Keutsch, F. N., Flagan, R. C., and Seinfeld, J. H.: Characterization of vapor wall loss in laboratory chambers, Environ. Sci. Technol, 44, 5074–5078, https://doi.org/10.1021/es100727v, 2010.

Marshall, F. H., Berkemeier, T., Shiraiwa, M., Nandy, L., Ohm, P. B., Dutcher, C. S., and Reid, J. P.: Influence of particle viscosity on mass transfer and heterogeneous ozonolysis kinetics in aqueous–sucrose–maleic acid aerosol, Phys. Chem. Chem. Phys., 20, 15 560–15 573, https://doi.org/10.1039/C8CP01666F, 2018.

Müller, J. F., Peeters, J., and Stavrakou, T.: Fast photolysis of carbonyl nitrates from isoprene, Atmos. Chem. Phys., 14, 2497–2508, https://doi.org/10.5194/acp-14-2497-2014, 2014.

Nah, T., Sanchez, J., Boyd, C. M., and Ng, N. L.: Photochemical Aging of α-pinene and β-pinene Secondary Organic Aerosol formed from Nitrate Radical Oxidation, Environ. Sci. Technol., 50, 222–231, https://doi.org/10.1021/acs.est.5b04594, 2016.

Nah, T., McVay, R. C., Pierce, J. R., Seinfeld, J. H., and Ng, N. L.: Constraining uncertainties in particle-wall deposition correction during SOA formation in chamber experiments, Atmos. Chem. Phys., 17, 2297–2310, https://doi.org/10.5194/acp-17-2297-2017, 2017.

Ng, N. L., Chhabra, P. S., Chan, A. W. H., Surratt, J. D., Kroll, J. H., Kwan, A. J., McCabe, D. C., Wennberg, P. O., Sorooshian, A., Murphy, S. M., Dalleska, N. F., Flagan, R. C., and Seinfeld, J. H.: Effect of NOx level on secondary organic aerosol (SOA) formation from the photooxidation of terpenes, Atmos. Chem. Phys., 7, 5159–5174, https://doi.org/10.5194/acp-7-5159-2007, 2007.

Ng, N. L., Brown, S. S., Archibald, A. T., Atlas, E., Cohen, R. C., Crowley, J. N., Day, D. A., Donahue, N. M., Fry, J. L., Fuchs, H., Griffin, R. J., Guzman, M. I., Herrmann, H., Hodzic, A., Iinuma, Y., Jimenez, J. L., Kiendler-Scharr, A., Lee, B. H., Luecken, D. J., Mao, J., McLaren, R., Mutzel, A., Osthoff, H. D., Ouyang, B., Picquet-Varrault, B., Platt, U., Pye, H. O. T., Rudich, Y., Schwantes, R. H., Shiraiwa, M., Stutz, J., Thornton, J. A., Tilgner, A., Williams, B. J., and Zaveri, R. A.: Nitrate radicals and biogenic volatile organic compounds: oxidation, mechanisms, and organic aerosol, Atmos. Chem. Phys., 17, 2103–2162, https://doi.org/10.5194/acp-17-2103-2017, 2017.

Nguyen, T. B., Crounse, J. D., Teng, A. P., St. Clair, J. M., Paulot, F., Wolfe, G. M., and Wennberg, P. O.: Rapid deposition of oxidized biogenic compounds to a temperate forest, Proc. Natl. Acad. Sci. USA, 112, E392, https://doi.org/10.1073/pnas.1418702112, 2015.

Odum, J. R., Hoffmann, T., Bowman, F., Collins, D., Flagan, R. C., and Seinfeld, J. H.: Gas/particle partitioning and secondary organic aerosol yields, Environ. Sci. Technol., 30, 2580–2585, https://doi.org/10.1021/es950943+, 1996.

Pankow, J. F.: An absorption model of gas-particle partitioning of organic-compounds in the atmosphere, Atmos. Env., 28, 185–188, 1994.

Perring, A. E., Pusede, S. E., and Cohen, R. C.: An Observational Perspective on the Atmospheric Impacts of Alkyl and Multifunctional Nitrates on Ozone and Secondary Organic Aerosol, Chem. Rev., 113, 5848–5870, https://doi.org/10.1021/cr300520x, 2013.

760 Pöschl, U.: Atmospheric aerosols: Composition, transformation, climate and health effects, Angew. Chem. Int. Ed., 44, 7520–7540, https://doi.org/10.1002/anie.200501122, 2005.

Press, W. H., Teukolsky, S. A., Vetterling, W. T., and Flannery, B. P.: Numerical Recipes 3rd Edition: The Art of Scientific Computing, Cambridge University Press, 2007.

Reid, J. P., Bertram, A. K., Topping, D. O., Laskin, A., Martin, S. T., Petters, M. D., Pope, F. D., and Rovelli, G.: The viscosity of atmospher-
765 ically relevant organic particles, Nature Comm., 9, 956, https://doi.org/10.1038/s41467-018-03027-z, 2018.

Roldin, P., Eriksson, A. C., Nordin, E. Z., Hermansson, E., Mogensen, D., Rusanen, A., Boy, M., Swietlicki, E., Svenningsson, B., Zelenyuk, A., and Pagels, J.: Modelling non-equilibrium secondary organic aerosol formation and evaporation with the aerosol dynamics, gas- and particle-phase chemistry kinetic multilayer model ADCHAM, Atmos. Chem. and Phys., 14, 7953–7993, https://doi.org/10.5194/acp-14-7953-2014, 2014.

770 Saunders, S. M., Jenkin, M. E., Derwent, R. G., and Pilling, M. J.: Protocol for the development of the Master Chemical Mecha-nism, MCM v3 (Part A): tropospheric degradation of non-aromatic volatile organic compounds, Atmos. Chem. Phys., 3, 161–180, https://doi.org/10.5194/acp-3-161-2003, 2003.

Seinfeld, J. H. and Pandis, S. N.: Atmos. Chem. Phys.: From Air Pollution to Climate Change, John Wiley & Sons, Inc., New York, 2016.

Shiraiwa, M., Pfrang, C., and Pöschl, U.: Kinetic multi-layer model of aerosol surface and bulk chemistry (KM-SUB): the influence of interfa-
775 cial transport and bulk diffusion on the oxidation of oleic acid by ozone, Atmos. Chem. Phys., 10, 3673–3691, https://doi.org/10.5194/acp-10-3673-2010, 2010.

Shiraiwa, M., Ammann, M., Koop, T., and Pöschl, U.: Gas uptake and chemical aging of semisolid organic aerosol particles, Proc. Natl. Acad. Sci. USA, 108, 11 003–11 008, https://doi.org/10.1073/pnas.1103045108, 2011.

Shiraiwa, M., Pfrang, C., Koop, T., and Pöschl, U.: Kinetic multi-layer model of gas-particle interactions in aerosols and clouds (KM-
780 GAP): linking condensation, evaporation and chemical reactions of organics, oxidants and water, Atmos. Chem. Phys., 12, 2777–2794, https://doi.org/10.5194/acp-12-2777-2012, 2012.

Shiraiwa, M., Yee, L. D., Schilling, K. A., Loza, C. L., Craven, J. S., Zuend, A., Ziemann, P. J., and Seinfeld, J. H.: Size dis-tribution dynamics reveal particle-phase chemistry in organic aerosol formation, Proc. Natl. Acad. Sci. USA, 110, 11 746–11 750, https://doi.org/10.1073/pnas.1307501110, 2013.

785 Takeuchi, M. and Ng, N. L.: Chemical composition and hydrolysis of organic nitrate aerosol formed from hydroxyl and nitrate radical oxidation of α-pinene and β-pinene, Atmos. Chem. Phys., 19, 12 749–12 766, https://doi.org/10.5194/acp-19-12749-2019, 2019.

Tikkanen, O. P., Hämäläinen, V., Rovelli, G., Lipponen, A., Shiraiwa, M., Reid, J. P., Lehtinen, K. E. J., and Yli-Juuti, T.: Optimization of process models for determining volatility distribution and viscosity of organic aerosols from isothermal particle evaporation data, Atmos. Chem. Phys., 19, 9333–9350, https://doi.org/10.5194/acp-19-9333-2019, 2019.

790 Ullmann, D. A., Hinks, M. L., Maclean, A. M., Butenhoff, C. L., Grayson, J. W., Barsanti, K., Jimenez, J. L., Nizkorodov, S. A., Kamal, S., and Bertram, A. K.: Viscosities, diffusion coefficients, and mixing times of intrinsic fluorescent organic molecules in brown limonene secondary organic aerosol and tests of the Stokes–Einstein equation, Atmos. Chem. Phys., 19, 1491–1503, https://doi.org/10.5194/acp-19-1491-2019, 2019.

Vaden, T. D., Imre, D., Beranek, J., Shrivastava, M., and Zelenyuk, A.: Evaporation kinetics and phase of laboratory and ambient secondary
795 organic aerosol, Proc. Natl. Sci. Acad. USA, 108, 2190–2195, https://doi.org/10.1073/pnas.1013391108, 2011.

Virtanen, A., Joutsensaari, J., Koop, T., Kannosto, J., YliPirilä, P., Leskinen, J., Mäkelä, J. M., Holopainen, J. K., Pöschl, U., Kulmala, M., Worsnop, D. R., and Laaksonen, A.: An amorphous solid state of biogenic secondary organic aerosol particles, Nature, 467, 824–827, https://doi.org/doi:10.1038/nature09455, 2010.

Yeh, G. K. and Ziemann, P. J.: Gas-Wall Partitioning of Oxygenated Organic Compounds: Measurements, Structure–Activity Relationships, and Correlation with Gas Chromatographic Retention Factor, Aerosol Sci. Tech., 49, 727–738, https://doi.org/10.1080/02786826.2015.1068427, 2015.

Yli-Juuti, T., Pajunoja, A., Tikkanen, O.-P., Buchholz, A., Faiola, C., Väisänen, O., Hao, L., Kari, E., Peräkylä, O., Garmash, O., Shiraiwa, M., Ehn, M., Lehtinen, K., and Virtanen, A.: Factors controlling the evaporation of secondary organic aerosol from α-pinene ozonolysis, Geophys. Res. Lett., 44, 2562–2570, https://doi.org/10.1002/2016GL072364, 2017.

Zaveri, R. A., Easter, R. C., Fast, J. D., and Peters, L. K.: Model for Simulating Aerosol Interactions and Chemistry (MOSAIC), J. Geophys. Res. Atmospheres, 113, https://doi.org/10.1029/2007jd008782, 2008.

Zaveri, R. A., Easter, R. C., Shilling, J. E., and Seinfeld, J. H.: Modeling kinetic partitioning of secondary organic aerosol and size distribution dynamics: representing effects of volatility, phase state, and particle-phase reaction, Atmos. Chem. Phys., 14, 5153–5181, https://doi.org/10.5194/acp-14-5153-2014, 2014.

Zaveri, R. A., Shilling, J. E., Zelenyuk, A., Liu, J., Bell, D. M., D'Ambro, E. L., Gaston, C. J., Thornton, J. A., Laskin, A., Lin, P., Wilson, J., Easter, R. C., Wang, J., Bertram, A. K., Martin, S. T., Seinfeld, J. H., and Worsnop, D. R.: Growth Kinetics and Size Distribution Dynamics of Viscous Secondary Organic Aerosol, Environ. Sci. Technol., 52, 1191–1199, https://doi.org/10.1021/acs.est.7b04623, 2018.

Zhang, X., Schwantes, R. H., McVay, R. C., Lignell, H., Coggon, M. M., Flagan, R. C., and Seinfeld, J. H.: Vapor wall deposition in Teflon chambers, Atmos. Chem. Phys., 15, 4197–4214, https://doi.org/10.5194/acp-15-4197-2015, 2015a.

Zhang, Y., Sanchez, M. S., Douet, C., Wang, Y., Bateman, A. P., Gong, Z., Kuwata, M., Renbaum-Wolff, L., Sato, B. B., Liu, P. F., Bertram, A. K., Geiger, F. M., and Martin, S. T.: Changing shapes and implied viscosities of suspended submicron particles, Atmos. Chem. Phys., 15, 7819–7829, https://doi.org/10.5194/acp-15-7819-2015, 2015b.

Ziemann, P. J. and Atkinson, R.: Kinetics, products, and mechanisms of secondary organic aerosol formation, Chem. Soc. Rev., 41, 6582–6605, https://doi.org/10.1039/c2cs35122f, 2012.